

Measurement Report: New particle formation characteristics at an urban and a mountain station in Northern China

Ying Zhou¹, Simo Hakala², Chao Yan^{1,2,*}, Yang Gao³, Xiaohong Yao³, Biwu Chu⁴, Tommy Chan², Juha Kangasluoma^{1,2}, Shahzad Gani², Jenni Kontkanen², Pauli Paasonen², Yongchun Liu¹, Tuukka Petäjä^{2,5}, Markku Kulmala^{1,2}, Lubna Dada^{2,6,7*}

¹ Aerosol and Haze Laboratory, Beijing Advanced Innovation Center for Soft Matter Science and Engineering, Beijing University of Chemical Technology, Beijing, China

² Institute for Atmospheric and Earth System Research / Physics, Faculty of Science, University of Helsinki, Finland

³ Key Laboratory of Marine Environment and Ecology, Ministry of Education, Ocean University of China, Qingdao 266100, China

⁴ State Key Joint Laboratory of Environment Simulation and Pollution Control, Research Center for Eco-Environmental Sciences, Chinese Academy of Sciences, Beijing 100085, China

⁵ Joint International Research Laboratory of Atmospheric and Earth System Sciences (JirLATEST), Nanjing University, Nanjing, China

⁶ Extreme Environments Research Laboratory, Ecole Polytechnique Fédérale de Lausanne (EPFL) Valais Wallis, Sion, 1951, Switzerland

⁷ Laboratory of Atmospheric Chemistry, Paul Scherrer Institute, 5232 Villigen, Switzerland

*Correspondence to: Lubna Dada: lubna.dada@helsinki.fi & Chao Yan: chao.yan@helsinki.fi

Abstract

Atmospheric new particle formation (NPF) events have attracted increasing attention for their contribution to the global aerosol number budget, and therefore their effects on climate, air quality, and human health. NPF events are regarded as a regional phenomenon, occurring over a large area. However, the Most observations on NPF events in Beijing and its vicinity were conducted in populated areas, whereas observations on NPF events in mountain with

few anthropogenic emissions are still rare in Beijing (Wang et al. 2013). The spatial variation of NPF event intensity has not been investigated in detail by incorporating both urban area and regional mountain measurements. Urban environments have more heterogeneous and freshly emitted NPF precursors as compared to environments with less anthropogenic activity in Beijing. Here, we provide provided NPF events characteristics in summer 2018 and 2019 at urban Beijing and a comparison of NPF event characteristics — NPF event frequency, particle formation rate, and growth rate — by comparing an urban Beijing site and a background mountain site separated by ~80 km from June 14 to July 14, 2019 as well as give insights into the connection between both locations. During the measurement period, 12 and 13 NPF events were observed at the urban and background mountain sites, respectively, with 9 NPF events observed on the same day at both sites. Although There were no significant difference of particle formation rates and growth rates observed during the short-term observation in 2019 and longer-term observation in summer 2018 and 2019 at the urban site. During parallel measurements at urban Beijing and mountain background areas, although the median condensation sink during the first two hours of the common NPF events was around 0.01 s^{-1} at both sites, there were notable differences in particle formation rates between the two locations (median of $5.42 \text{ cm}^{-3}\text{s}^{-1}$ at the urban site and $1.13 \text{ cm}^{-3}\text{s}^{-1}$ at the mountain site during the first two hours of common NPF events). Yet In addition, the particle growth rates in the 7-15 nm range for common NPF events were comparable at urban site (median of 7.6 nm.h^{-1}) at the urban site and 6.5 nm.h^{-1} at the were slightly higher than those at mountain site as (median values of 6.5 nm.h^{-1}). To understand whether the observed events were connected, we compared air mass trajectories as well as meteorological conditions at both stations. Favorable conditions for the occurrence of regional NPF events were largely affected by air mass transport. Overall, our results demonstrate a clear inhomogeneity of regional NPF within a distance of ~100 km, which should be considered in regional-scale aerosol models when estimating the budget of aerosol load and cloud condensation nuclei, possibly due to the discretely distributed emission sources.

Keywords: atmospheric aerosols, growth rates, regional new particle formation, haze, sulfuric

acid

1 Introduction

Atmospheric new particle formation (NPF) events resulting from the formation of clusters and stable aerosol particles from gas-phase precursors have been recognized as a major contributor to the global aerosol budget (Kulmala et al., 2004; Zhang et al., 2012). Once the newly formed particles grow to certain sizes, they can act as cloud condensation nuclei (CCN), affecting the regional and global climate (Pierce and Adams., 2009; Yu and Luo., 2009). NPF events were also found to contribute to haze formation and thus can influence air quality, especially in megacities where the precursor concentrations and associated particle formation rates are rather high (Guo et al., 2014; ~~Guo et al.,~~ 2020; Kulmala et al., 2021; Du & Dada et al., 2021).

The occurrence of NPF events is a result of the competition between factors promoting and inhibiting cluster formation and their growth. For instance, sufficient sulfuric acid and other low-volatility vapors have been confirmed to be important in particle nucleation and growth in field observations as well as in chamber experiments (Ehn et al., 2014; Wang et al., 2017; Lehtipalo et al., 2018; Yao et al., 2018; Deng et al., ~~2020a~~2020b). On the other hand, background particles can inhibit new particle formation by acting as condensation sink for vapor precursors and coagulation sink for newly formed particles. Indeed, Cai et al. (2017) found that the Fuchs Surface Area (A_{Fuchs}) (which is linearly proportional to condensation sink) determined the occurrence of NPF events in urban Beijing. In the atmosphere, ambient conditions, such as air mass trajectories and meteorological conditions, can affect the occurrence of NPF events by modifying the source-sink competition. Wu et al. (2007) summarized favorable conditions for NPF events in Beijing based on a one-year observation as sufficient solar radiation (sunny days), northerly wind, low relative humidity, and less pre-loading large particles. Similarly, in other environments, plenty of radiation, intermediate temperatures and low condensation sink favor the occurrence of NPF events (Qi et al., 2015; Dada et al., 2017; Kerminen et al., 2018). Regional NPF events can happen with a spatial extent up to several hundred kilometers and vertical extent from boundary layer to free

troposphere under favorable conditions (Hussein et al., 2009; Shen et al., 2011; Dai et al., 2017). Earlier studies have shown that regional NPF events by simultaneous observations at two or more sites had similar features in their occurrence and characteristics. For instance, Komppula et al. (2006) investigated the occurrence of NPF events at two forest stations in northern Finland during 2000-2003. Their results suggested that same air mass source regions, favorable weather conditions and clean air at both stations were necessary for NPF events occurring simultaneously at the two stations. Vana et al. (2016) compared observations at three sites over 1000 km distance at northern Finland, southern Finland and Estonia in 2013-2014. They found that some events have the same origin. On the other hand, Jun et al. (2014) observed that NPF events occurred less frequently at downtown Toronto than at a nearby background site, and attributed this observation to the high condensation and coagulation sink due to primary particle emission from traffic at urban areas. Moreover, Carnerero et al. (2018) observed horizontal distribution and regional impact of the NPF events with data from three urban, urban background, and suburban stations in the Madrid metropolitan area, Spain in July 2016. Their results indicated that ultra-fine particles were detected quasi-homogenously in an area spanning at least 17 km horizontally and the NPF events extended over the full vertical extension of the mixed layer. Finally, Salma et al. (2016) found that regional NPF events were modified and transformed by urban NPF events during their observation in 2008-2009 and 2012-2013 in Budapest and at a regional background site 71 km away from it.

In comparison to the aforementioned studies in Europe, a similar study was also carried out to understand the regional NPF events in North China Plain. Wang et al. (2013) characterized the NPF events observed at an urban Beijing site and a regional background site about 120 km northeast to the urban site from March to November in 2008. They observed 96 and 87 NPF events at urban Beijing and background site, respectively, among which 52 NPF events were observed simultaneously at both sites. They found that NPF events were slightly weaker in the background site compared to those observed at the urban site. However, the factors that influence the occurrence of NPF events at the two stations simultaneously were left

undetermined. In addition to largely populated urban areas, there is a large mountain area within the Beijing-Tianjin-Hebei (BTH) region, where to our best knowledge, the characteristics of NPF events are understudied. In this study, we conducted simultaneous measurements of NPF event characteristics at an urban site in Beijing and a background mountain site about 80 km west to urban Beijing from June 14 to July 14 2019. Based on our observations, we aim to (i) compare the characteristics of the NPF events between the two sites, including the frequency, particle formation rate, and particle growth rate; (ii) figure out the connections and differences between NPF events at these two sites; (iii) identify the favoring conditions for regional NPF events. Due to the profound participation of NPF events in the global aerosol number loading and air quality degradation, identifying the conditions that promote or inhibit the occurrence of regional scale NPF events could help minimize its adverse effects.

2 Experiment and methodology

2.1 Sites' description

Urban site: The Beijing University of Chemical Technology - BUCT (39.94° N, 116.31° E) station is located on the fifth floor of a university building inside the west campus of BUCT. The station is surrounded by several main roads with heavy traffic and residential areas and thus, can be considered a typical urban station. More details of this station can be found in Zhou et al. (2020). Observations at the urban site are continuous since January 17, 2018 and were only interrupted for necessary instrument maintenance. The location is referred to as 'UB' from here after and is shown on the map in Fig. 1.

Mountain site: The Beijing Forest Ecosystem Research Station (39.96° N, 115.43° E) is located in the west of Beijing, referred to as 'MT' from here after, which is part of the Chinese Ecological Research Network (CERN). It is located in the mountain areas west of Beijing, about 80 km from the urban site; see also in Fig. 1. The altitude of the station is 1170 m above sea level and it is surrounded by forests. The closest anthropogenic activities are associated with small villages located in the valley nearby the MT station. Observations at

MT station are from June 14 to July 14, 2019. For comparison reasons, we only used the data collected simultaneously at both stations.

2.2 Instrumentation

Particle number size distribution data in the size range of 6-840 nm were collected using a differential mobility particle sizer (DMPS) at the UB station. The instrument consists of one Hauke-type DMA (differential mobility analyzer, home-built by university of Helsinki) in different flow rates and one CPC (condensation particle counter, TSI Model 3772). Details of this instrument can be found in Salma et al., 2011 and Kangasluoma et al. (2020). At MT station, a scanning mobility particle sizer (SMPS, consists of a TSI Differential Mobility Analyzer model 3081) and a fast mobility particle sizer (FMPS, TSI Model 3091) were used to measure particle number size distribution from June 14 to June 28 and from June 29 to July 14, respectively. The size ranges of the SMPS and FMPS are 7-1218 nm and 6.04-856 nm, respectively. The total number concentration from 4-3000 nm, measured by Condensation Particle Counter (CPC; TSI Model 3775), was used to calibrate the particle number size distributions from FMPS according to the method suggested by Zimmerman et al. (2015). More details about the instrument are found in the previous studies (Wang et al., 2019; Gao et al., 2020). The full campaign particle number size distributions at both sites are shown in Fig. 2. The particle number size distribution measured by FMPS correlated well with SMPS after being calibrated (Lee et al., 2013).

To ensure high quality of particle number size distribution data at UB site, a particle number size distribution system (PSD) also sampled in parallel with DMPS from June 1 to August 31, 2019 (summer 2019). It included a nano-scanning mobility particle sizer (nano-SMPS, 3–55 nm, mobility diameter), a long SMPS (25–650 nm, mobility diameter) and an aerodynamic particle sizer (APS, 0.55–10 μ m, aerodynamic diameter). Details of this instrument can be seen at Liu et al. (2016) and Deng et al. (2020b).

As shown in Fig.3, median particle number size distribution obtained from PSD and DMPS matched well with each other within a factor of 2 during our observation in summer 2018 and

2019 at UB site. We cannot compare particle number size distribution data obtained from DMPS, SMPS and FMPS as we did not sample with these three instruments in parallel at the same site. However, it is reasonable to assume that particle number size distribution obtained from FMPS were comparable with those from DMPS as on one hand the measurement techniques of particle number size distribution in the size range of these two instruments have been well developed and been applied in quite a lot of observations (Wang et al., 2017; Kangasluoma et al., 2020), on the other hand, the FMPS was carefully calibrated and properly operated during the observation as discussed above. Similar conclusions apply for the SMPS as well where we can rely on using the measurement from this instrument to discuss at least NPF event frequency at MT site during June 14 to June 28, 2019, during which parameters of only one NPF event are calculated.

Sulfur dioxide (SO₂) concentration data were collected by Thermo Environmental Instrument model 43i-TLE with a time resolution of 5-min at the UB station. There were no direct measurement of SO₂ concentrations at the MT station, but the SO₂ measurement at the closest national monitoring station (Longquan station, around 60 km from MT station and 20 km from UB station, see Fig. 1) was used to indicate the strong decline of SO₂ concentration from urban Beijing towards the west areas. Time series of SO₂ concentration at UB station and Longquan station during the whole observation is shown in Fig. 34. Due to the lower emission, the SO₂ concentration at the MT station is expected to be even lower than that in Longquan station.

The sulfuric acid concentration was measured at UB station by a chemical ionization-atmospheric interface-time of flight mass spectrometers (CI-APi-ToF, Aerodyne Research Inc.) equipped with a nitrate chemical ionization at UB station (Lu et al., 2019). There were no sulfuric acid data available at MT station and since no SO₂ concentrations were available, a sulfuric acid proxy concentration could not be derived.

The meteorological conditions such as relative humidity (RH, %), temperature (°C) and solar radiation (UVA and UVB, W/m²) were measured using a Vaisala Weather station data acquisition system (AWS310, PWD22, CL51), Metcon at UB station and using Vaisala

MAWS301 automatic weather station at MT station. The measurements at the MT station were carried out at the height of 1.5 m. The wind speed (m/s) and wind direction (°) data is also measured by the weather station at UB site, while at MT site, we obtained with reanalyzed data from ERA5 model (Olauson, 2018).

2.3 Air mass back trajectories

Air mass back trajectories were calculated using a Lagrangian particle dispersion model FLEXPART (FLEXible PARTicle dispersion model) version 9.02 (Stohl et al., 2005). As the meteorological input, we used ECMWF (European Centre for Medium-Range Weather Forecast) operational forecast data with 0.15° horizontal and 1-hour temporal resolution. Particle retroplume simulations were performed hourly for both sites during the whole study period. For each retroplume simulation, we used 50 000 model particles distributed evenly between 0–100 m above the measurement site. The released model particles were traced backwards in time for 72 h, unless they exceeded the model grid (20–60°N, 95–135°E, resolution: 0.05°).

Based on the arrival direction of the 72-h backward trajectories, the prevailing air mass transport conditions at each site were classified into 5 groups: North group, West group, East group, South group and Local group. Air masses arriving from north, north-west and north-east including Mongolia, Inner-Mongolia and north-east China were classified into the North group. Air masses from Shanxi province, Inner-Mongolia and further west were classified into the West group. Air masses from the ocean east of Beijing were classified into the East group and air masses from southern areas were classified into the South group. Stagnant air masses that had only travelled short distances and/or were circulating around the measurement site were classified into the Local group. Examples of air mass trajectories belonging to these five groups are shown in Fig. 4.5. In general, air masses from the north and west supply clean air from the mountainous areas to both stations, whereas air masses from the east and south travel over highly populated areas, thus accumulating air pollutants. However, the impact of local air masses on the pollution levels at the two sites can be

different; at UB station, local air masses are polluted by the urban emissions, while at MT station stagnant air could cause a clean situation due to low local emissions. More details on the relationship between air mass transport conditions and the extent of pollution is discussed in later sections.

2.4 Estimating the spatial extent of NPF

The observation of regional new particle formation events, where the growth of newly formed particles can be followed for several hours, is a result of NPF taking place over a large spatial area. This is because as time progresses, the particles observed at a measurement site must have originated from further and further away due to non-zero wind conditions. Following the progression of the observed NPF event and using air mass back trajectories, we can estimate where the particles observed at different stages of the NPF event were initially formed by calculating the air mass locations at the onset time of the NPF event (assuming that NPF occurs simultaneously over the larger area). Typically, the mode related to the NPF event disappears from the observations after some time. This is an indication of the currently observed air mass arriving from an area where NPF was no longer taking place due to unfavorable local conditions. If the shift in the air mass origin towards unfavorable conditions occurs gradually over time, the mode related to the NPF event can enter a stage of growth stagnation (or even decrease in size) before disappearing completely (Kivekäs et al., 2016). This is because the increasing transport time between NPF onset and observation of the particles at the measurement site provides less and less additional ‘material’ for aerosol growth towards the more unfavorable conditions. Calculating the locations where NPF is assumed to have taken place for longer data sets including several regional NPF events can give an estimation of the typical spatial extent of NPF around the measurement location. It should be noted that even in relatively clear cases, the subjective determination of NPF event onset and end times can easily lead to uncertainties of few tens of kilometers in the estimations. In locations with strong primary pollution sources, such as urban Beijing, objective determination of said times becomes even more difficult. More details and discussion related to the method and its uncertainties can be found in Kristensson et al.

(2014).

2.4 NPF event classification

Particle number size distribution data from both stations were used for classifying individual days into new particle formation (NPF) event days and non-event days. This classification followed procedures presented by Dal Maso et al. (2005) and later adapted for urban locations (Chu et al., 2021) in which a day is classified as a NPF event day if (a) a new mode in the size range smaller than 25 nm appeared and (b) the new mode kept growing over several hours. On the other hand, non-event days are the days which do not fit any of the abovementioned criteria and undefined days are the days which fit either one of the abovementioned criteria or the days which we cannot distinguish whether the new mode was from NPF event or traffic.

2.5 Characteristics of NPF events

2.5.1 Condensation sink

The condensation sink (CS) was calculated from particle size distribution data using the method described by Kulmala et al. (2012):

$$CS = 2\pi D \sum_{dp'} \beta_{m,dp'} dp' N_{dp'}$$

(1)

where D is the diffusion coefficient of the condensing vapor, sulfuric acid in our case, and $\beta_{m,dp'}$ represents the transition-regime correction, $N_{dp'}$ is the particle number concentration with diameter dp' . As shown in Fig. 56, particles in size range of 20-800 nm dominated the total CS at UB station and particles in the size range of 50-800 nm dominated the total CS at MT station. Although the size ranges of DMPS, FMPS and SMPS slightly differ, all of them cover the main size range which constituted the CS and thus the calculation of CS should not be significantly influenced by differences in the instrument size ranges.

2.5.2 Particle growth rates

Particle growth rates were calculated for the size range of 7-15 nm ($GR_{7-15\text{ nm}}$) using the 50% appearance time method introduced by Lehtipalo et al. (2014) and Dada et al. (2020a) according to

$$GR = \frac{dp_2 - dp_1}{t_2 - t_1} \quad (2)$$

where t_2 and t_1 are the appearance times of particles with sizes of dp_2 and dp_1 , respectively. The appearance time is defined as the time at which the concentration of particles at size d_p reaches 50% of its maximum.

2.5.3 Particle formation rates

The formation rates of particles of diameters 7 nm (J_7) were calculated from particle number size distribution data using the method presented by Kulmala et al. (2012) and modified for urban environments by Cai and Jiang (2017):

$$J_k = \frac{dN_{[d_k, d_u]}}{dt} + \sum_{d_g=d_k}^{d_u-1} \sum_{d_i=d_{\min}}^{+\infty} \beta_{(i,g)} N_{[d_i, d_{i+1})} - \frac{1}{2} \sum_{d_g=d_{\min}}^{d_u-1} \sum_{d_i^3=\max(d_{\min}^3, d_k^3-d_{\min}^3)}^{d_{i+1}^3+d_{g+1}^3 \leq d_u^3} \beta_{(i,g)} N_{[d_i, d_{i+1})} N_{[d_g, d_{g+1})} + \left. \frac{dN}{dd_i} \right|_{d_i=d_u} \bullet GR_u \quad (3)$$

Here, J_k is the particle formation rate at size d_k , $\text{cm}^3 \cdot \text{s}^{-1}$, (7 nm in this study); d_u is the upper size limit of the targeted aerosol population (10 nm in this study); d_{\min} is the smallest particle size detected by particle size spectrometers (to make the results comparable, the d_{\min} was set to 7 nm); $N_{[d_k, d_u]}$ is the number concentration of particles from size d_k to d_u ; d_i represents the lower limit of the i^{th} size bin; $\beta_{(i,g)}$ is the coagulation coefficient for the collision of two particles with the size of d_i and d_g ; and GR_u refers to the particle growth rate at size d_u , $\text{nm} \cdot \text{h}^{-1}$ (Deng et al., 2020a, (2020b)).

3 Results and discussion

3.1 NPF event ~~characteristics~~frequencies at both stations

During our observation in summer 2018 and 2019 (from June to August of each year) at UB station, there were 155 days with valid data, 53 days of which were classified as NPF event days, corresponding to an NPF event frequency of 34%. This NPF event frequency was consistent with observations in urban Beijing in 2004 and 2008 in summer while smaller than other seasons especially winter during those observations and the observation in UB station (Wu et al., 2007; Wang et al., 2013; Deng et al., NPF event frequency at both stations 2020b).

For comparison of NPF characters between UB and MT stations, a parallel short-term observation was conducted at MT station from June 15 to July 14, 2019. In Fig.-2, we show the particle number size distribution and CS during our short-term observations at both stations. There were a total of 12 and 13 NPF events observed at the UB station and the MT station, corresponding to an NPF event frequency of 48% (12 of 25) and 52% (13 of 25), respectively. ~~Only days when there was good data for both stations were taken into consideration in our whole analysis. The NPF event frequencies were higher than earlier long-term observations in urban Beijing and at a background site in Beijing, as well as another observation in 2018 at UB station in which NPF events occurred on less than 20% of the days in summer (Wang et al., 2013; Deng et al., 2020a). One possible reason could be that earlier observations covered the whole summer while our observation only lasted for 31 days (where 25 days were validated data), and some parameters affecting NPF event occurrence could vary from month to month as well as from year to year.~~Only days when particle number size distribution data were valid that visual inspection of the data and the number concentrations as well as instrument status do not indicate problems in the measurements for both stations were taken into consideration in our analysis. In addition, 9 NPF events were observed at both stations on the same day (referred to as common NPF events). Detailed information on the classified NPF event and non-event days, including the particle formation rates, growth rates, as well as their associated air mass origins during the short-term

observation are provided in Table 1.

3.1.1 NPF event start time at both stations

During our observation, there was no advection of air masses between the two sites on common NPF event days, indicating that the NPF events occurred at each site independently. As shown in Table 1, all common NPF events started after sunrise and prior to noon except the two non-local NPF events at MT station. However, NPF event start time was different between the two sites. Earlier researches in Nanjing, China and Nordic stations showed the similar results that NPF events can be observed simultaneously at two or more sites, but the start time can be different, local meteorology, source strength and background aerosols could drive temporal behavior of NPF events at each sites (Hussein et al., 2009; Dai et al., 2017).

3.1.2 Particle formation and growth rates at both stations

The particle formation rates (J_z) at the two stations during the measurements are shown in Fig.6a. The J_z at the UB station ($3.0\text{--}10.0\text{ cm}^{-3}\text{s}^{-1}$ with a median of $5.4\text{ cm}^{-3}\text{s}^{-1}$) was significantly higher than that in the MT station ($0.75\text{--}3.0\text{ cm}^{-3}\text{s}^{-1}$ with a median of $0.72\text{ cm}^{-3}\text{s}^{-1}$) for common NPF events. These values are comparable to earlier observations in urban Beijing and another regional background station in North China Plain (NCP) (Wang et al., 2013). Earlier observations in NCP and Yangtze River Plain also observed higher formation rates at urban sites than corresponding background sites by roughly a factor of 2 due to lower anthropogenic emissions at background sites (Wang et al., 2013; Dai et al., 2017; Shen et al., 2018). The much lower J_z observed at MT station is very likely associated with the low H_2SO_4 concentration at this station, which we will discuss in section 3.2.4. However, other reasons, such as the low concentration of H_2SO_4 stabilizers, e.g., amines, cannot be ruled out either. Also, the J_z at UB station could be affected by particle emissions due to the proximity of the location to the highway (Kontkanen et al., 2020).

In contrast to the significant difference of J_z , the median particle growth rates in size range of 7–15 nm ($\text{GR}_{7-15\text{nm}}$) were similar between the two stations, with 7.6 nm/h and 6.5 nm/h at the

UB station and the MT station, respectively (Fig. 6b). The GR at UB station was comparable with other long-term observation at UB station (1.1–8.0 nm/h) in 2018, and other urban areas in China (Herrmann et al., 2014; Chu et al., 2019; Deng et al., 2020a). Consistent with earlier observations showing that H_2SO_4 could only contribute to a small fraction of the particle growth at this size range (Paasonen et al., 2018; Qi et al., 2018; Guo et al., 2020), the growth rates at both stations cannot be explained by the H_2SO_4 concentration. This implies that other condensable species, very likely low volatility organic vapors, play an important role in particle growth at both stations. At the UB station, anthropogenic VOCs are dominant precursors of these low volatility organic vapors (Guo et al., 2020; Deng et al., 2020b), while VOCs at MT station, with rare anthropogenic sources, are likely dominated by biogenic emissions.

3.1.3 Ending diameters of newly formed grown particles

Earlier observations found that diameters of newly formed particles should be larger than 70 nm to contribute to cloud condensation nuclei significantly (Man et al., 2015; Ma et al., 2021) and will be considered as haze particles when their size larger than 100 nm (Kulmala et al., 2021). However as shown in Table 1, the maximum mode diameters of the newly grown particles ($D_{p\text{max}}$) varies from 21 to 105 nm at the UB station and 19 to 102 nm at MT station and $D_{p\text{max}}$ of common NPF events were higher at UB than MT station. At UB station there were 4 NPF events with $D_{p\text{max}}$ larger than 70 nm, while only one such event was observed at MT station. The higher ending diameters of the newly formed grown particles indicates more abundant vapors favoring the growth of larger particles at UB than MT station. The result also suggests that NPF events at urban areas may have larger impacts on haze and climate than those at clean areas.

3.2 Factors influencing the occurrence of NPF events

In order to understand the conditions favoring NPF events at both stations, we analyzed various ambient parameters including air mass trajectories, meteorological variables,

condensation sink as well as sulfuric acid concentration.

3.1.1 Favorable air mass origin for NPF events at individual locations

~~Due to the close proximity of the two measurement sites, the air mass arrival directions and source regions were (mostly) similar at both sites throughout the measurement period.~~
~~Frequencies~~In Fig.7, we show frequencies of air masses arriving at ~~each~~UB station from every group ~~are shown~~different directions during our observation in Fig. 7: ~~summer 2018 and 2019~~. The most frequent air masses arriving at ~~both sites~~UB station belonged to the ~~North and East groups~~. At the ~~UB site~~South group. During our observation in the two summers, out of ~~25~~155 days ~~there were~~ 852 days belonging to ~~each of the~~NorthSouth group and ~~East groups~~39, 32, 9 and ~~1, 1 and 7~~23 days in air masses ~~belonging~~belong to ~~North, East, West, South and Local groups, respectively~~. For the MT station, ~~there were out of 25 days, 9 and 6 belonged to the North and East groups, respectively, and 3 and 7 days belonged to West, Local groups, respectively.~~

NPF event frequency with respect to air masses is also shown in Fig. 7. It is noticeable that air mass origin influenced the occurrence of NPF events at ~~both stations~~UB site as the ~~highest frequency~~majority of NPF events occurred when the air masses were coming from the north. ~~The second highest frequency of NPF events was observed when the air mass belonged to the Local group (Fig. 7a&b).~~ At UB station, 11 (out of 12) NPF events occurred ~~in these two air mass classes (North and South groups), with another NPF event~~During our observation in the West group. For the MT station, ~~11~~summer 2018 and 2019, 34 (out of ~~13~~55) NPF events occurred in ~~these two air mass classes (masses from the North group and South groups), with two other~~9, 2, 2 and 6 NPF events in the ~~West and East groups~~. Considering the comparable NPF frequency associated with the North and South group, the difference in the CS remains one prominent difference between them. As shown in Fig. 7e&d, ~~South, East, West and Local groups, respectively (Fig.7a).~~ One prominent feature of these air masses is their difference in CS. ~~the~~The CS of the air masses classified as the North group (with median values of 0.01 s^{-1} at ~~both stations~~UB station) is substantially lower than that in other air mass classes, (CS = 0.03, 0.025, 0.017, 0.03 s^{-1} , for south, east, west and local,

respectively), which might be a main reason to explain the high NPF event frequency
associated with this air mass class. This result is consistent with earlier researches that air
masses from north favored NPF occurrence by low CS in North China Plain (Wang et al.,
2013; Shen et al., 2018). On the other hand, despite the highest CS of theDuring the
observation from June 14 to July 14 in summer 2019, the most frequent air masses in Local
arriving at both sites belonged to the North group as shown in Table 1. Out of 25 days, there
were 8 and 9 days belonging to the North group (with median values of 0.025 and 0.028 s⁻¹,
at the UB station and MT stations, respectively, on NPF event days), NPF event. The
highest frequency of NPF events also occurred when the air masses were coming from the
north. The high NPF events frequency during our observation from June 14 to July 14 could
still occur in this air mass class. This is likely due also be attributed to the high concentrations
of cluster forming vapors that act as particle sources outcompeting the high CS in these cases.
frequent air masses arriving at both sites from north to Beijing.

As shown in Table 1, NPF events occurring simultaneously at both sites only happened when
air masses arrived at both sites from the same directions, suggesting that most of the observed
NPF events took place over the whole studied area, extending for several hundreds of
kilometers (Dai et al., 2017; Du et al., 2021). The occurrences of common NPF events also
closely connected with air mass origins that 7 (out of 9) common NPF events occurred under
air masses in the North group, with the other two NPF events in the South group.

3.1.2 The role of the condensation sink in NPF event occurrence

Figure 8 shows the difference in CS on NPF event and non-event days at the two stations. On
NPF event days, Figure 8a shows the difference in CS between NPF event and non-event days
during our observation in summer 2018 and 2019 (two whole summers) at UB site and
short-term parallel observations at both sites. The ‘NPF1’ and ‘non-event1’ referred to NPF
and non-event days during the two whole summers, respectively, while ‘NPF2’ and
‘non-event2’ referred to NPF and non-event days during the short-term parallel observation
period from June 14 to July 14, 2019 at both sites, respectively. The longer-term periods are
used for confirming the representativeness of the short-term overlapping period for the whole

summer. As shown in the figure, the median CS on NPF1 or NPF2 days is equivalent for UB station ($CS_{NPF1} = 0.010s^{-1}$; $CS_{NPF2} = 0.009s^{-1}$) and less than a factor of 1.2 different between non-event1 and non-event2 in UB station ($CS_{nonevent1} = 0.023s^{-1}$; $CS_{nonevent2} = 0.020s^{-1}$), which confirms the representativeness of our short-term measurement period to the overall urban Beijing summer.

Our results in figure 8a show that the median CS was $\sim 0.01 s^{-1}$ during the first 2 hours of the NPF events, at both stations. On common NPF event days, the median CS was $0.009 s^{-1}$ at UB station and $\sim 0.01s^{-1}$ at MT station, respectively. In comparison, on non-event days, during roughly the same time period (9:00–11:00 LT), the CS was substantially higher, with median values of $0.02 s^{-1}$ and $0.014 s^{-1}$, at UB and MT stations, respectively. The median CS on NPF event days during our measurement period was lower than those previously reported values based on long-term data which was $0.027 s^{-1}$ and $0.019 s^{-1}$ at two sites in urban Beijing respectively (Figure 8b presents the median CS during the first 2 hours of NPF events on common NPF event days measured at both stations, and shows the high correlation between the two Wang et al., 2013; Deng et al., 2020a). This could be attributed to a shorter studied period in our study as well as changes in meteorological conditions in comparison to previous years.

As shown in Fig. 9a&b, when CS was smaller than $0.015 s^{-1}$, most (10 out of 11) days were classified as NPF event days. Figure 8c shows the frequency as a function of CS during our observation at UB site in summer 2018 and 2019 and how the NPF event frequency decreased with increasing CS. When CS was larger than $0.03201 s^{-1}$, all days were classified as non-event days. When CS was smaller than $0.03201 s^{-1}$, all days were NPF event days, and when CS was larger than $0.035 s^{-1}$, no day was classified as NPF event day. This shows the major role of background particles in controlling the occurrence or inhibition of NPF events as shown in several previous studies in China and internationally (Deng et al., 2020a; Cai et al., 2017; Kulmala et al., 2017). While we cannot present a similar figure from the MT station, the same conclusion applies where CS does play a role in inhibiting NPF observation owing to the difference in the CS values observed between 0.015 and $0.032 s^{-1}$, there were only 2 NPF event days, 4

~~undefined days and 4 non-event days. NPF and nonevents at MT as shown in figure 8a. Yet, since the overall preexisting particle concentration at the MT is rather on the low end, the role of CS might not be as vital at the MT station as for the UB station.~~

Different from NPF events under low CS ($<0.01501 \text{ s}^{-1}$), these ~~two~~ NPF events under high CS were characterized by a relatively high H_2SO_4 concentration ($>10^7 \text{ cm}^{-3}$) ~~and/or~~ low particle formation rates, (Fig.9a), discussed in further details in the coming sections. ~~This result is consistent with long-term observations at UB station during 2018 (Jan 16–May 17 and Oct19–Dec 26) and 2019 (Jan 1–Mar 28 and Jul 19–Dec 31) (Deng et al., 2020a). As well as at another site in urban Beijing during 2016 (Mar 7–Apr 6) during which NPF event days dominated the measured days when CS was smaller than 0.01 s^{-1} , and NPF events rarely happened when CS was larger than $\sim 0.03 \text{ s}^{-1}$ (Deng et al., 2020a).~~ In comparison, at MT station, when CS was smaller than $\sim 0.013 \text{ s}^{-1}$, most (10 out of 14) days were classified as NPF event days as shown in Fig. 9d. When CS was larger than $\sim 0.013 \text{ s}^{-1}$, we only observed one local NPF event and another two non-local NPF events (~~the non-local NPF events will be discussed in section 3.3.2). Table 1~~). The local NPF event under high CS at the MT station was characterized as high UV ($>30 \text{ W/m}^2$) and low formation rate (J_7 were too small to be reliably calculated) as well.

3.1.3 Role of meteorological variables in NPF event occurrence

While the air mass source regions, and their connection to the CS, seem to explain the general picture of NPF event occurrences at the two sites well, we still have some cases unexplained. For example, as shown in Table 1, there were several non-event days observed at MT station with air masses belonging to North and West groups, which were connected to low CS. This indicates that a further investigation into other NPF-related variables is still required.

In Figure 10, we show diurnal variation of meteorological variables during our observation in summer 2018 and 2019 at UB site and observations from June 14 to July 14 in 2019 at UB and MT sites. It is noticeable that the short-term observation compared well with the long-term observation and therefore is representative of summer at UB site as shown in Fig.10.

First, the intensity of solar radiation is considered one of the most important parameters deciding NPF event occurrence as it translates into photochemistry strength (Chu et al., 2019). The median UV (UVA+UVB) intensity at the UB station on NPF event and non-event days was 38.3 and 32.9 W/m², respectively. The UV intensity was on average ~15% higher on NPF event days than on non-event days at UB station. Although UV intensity was important for NPF event occurrence, we still observed NPF events at UB station under low UV intensity, e.g. cases on June 30 and July 6 ~~as shown in Fig. 9a.~~ These two events all started immediately after sunrise (6:30 LT on June 30 and 7:00 LT on July 6, see Table 1) and median UV intensity during the first two hours of NPF events was only 13.2 and 14.1 W/m² ~~(Fig. 9b).~~, respectively. However, sulfuric acid concentration was higher than 10⁷ cm⁻³ at the same time, the possible reason is high SO₂ concentration and low CS (~0.003 s⁻¹, ~~see Fig. 9a~~) outcompeted the low UV intensity (Dada et al., ~~2020a~~2020b) as well as the possibility of having other H₂SO₄ sources (Yao et al., 2020).–

At MT station, the median UV intensity on NPF event and non-event days was 28.4 and 14.2 W/m², respectively. The lower UV at MT station, in general might be related to the higher RH (Fig. 10c&d) and thus more cloudiness and fog at the MT station (Hamed et al., 2010; Dada et al., 2018). The UV intensity was on average ~100% higher on NPF event days than on non-event days at UB station. All local NPF events happened when UV intensity was higher than 15 W/m² as shown in Fig. ~~9e~~9d.

On the other hand, as shown in Fig. 10c&d, the median relative humidity (RH) was lower on NPF event days than non-event days at both stations. This is consistent with earlier results that high RH suppressed NPF events by increasing CS and coagulation sink (CoagS), as it can enhance the particle hygroscopic growth (Hamed et al., 2010; Hamed et al., 2011). In addition, high RH was also found to be associated with more clouds resulting in less solar radiation (Dada et al., 2018).

The median temperatures at UB on event and non-event days were 31 °C and 29 °C, respectively, and at MT station 23 °C and 19 °C, respectively. The median temperature was lower at the MT station than at the UB station, due to the higher altitude of the station and

likely also the weaker solar radiation (Fig. 10a&b10e&f). At both stations, the median temperature was very similar on NPF event and non-event days, suggesting that temperature was not a crucial factor for NPF event occurrence during the measurement in summer.

3.1.4 Role of Sulfuric acid concentrations in NPF event occurrence

Besides having favorable conditions such as low CS and sufficient radiation, the occurrence of NPF event requires a sufficient concentration of precursor vapors. Sulfuric acid has been found to be the main precursor vapour participating in NPF in China and in many locations around the world due to its low volatility (Yao et al., 2018; Chu et al., 2019; Yao et al., 2018). In Fig. 9a&b, we show the concentration of sulfuric acid as a function of CS during summer 2018 and 2019 at UB site. As shown in Fig. 9e9b, the median sulfuric acid (H_2SO_4) concentrations at UB station were $8.1 \times 10^6 \text{ cm}^{-3}$ and $4.5 \times 10^6 \text{ cm}^{-3}$ on NPF event days and non-event days, respectively, during observation from June 14 to July 14 in 2019 and $7.9 \times 10^6 \text{ cm}^{-3}$ and $3.4 \times 10^6 \text{ cm}^{-3}$ on NPF event days and non-event days, respectively, during the observation in summer 2018 and 2019. This suggests that H_2SO_4 was important for NPF events at the UB station (Deng et al., 2020a; 2020b; Dada et al., 2020a; 2020b). On the other hand, as shown in Fig. 9e9a, the H_2SO_4 concentration during 9:00- 11:00 (local time) on non-event days could be comparable with that on NPF event days, especially when CS was high. The H_2SO_4 concentration during 9:00- 11:00 (local time) on non-event days could be comparable with that on NPF event days, especially when CS was high. Altogether, our observation shows that the occurrence of NPF events was controlled by both H_2SO_4 and CS at the UB station (Cai et al., 2020).—

In addition, although we did not perform the measurement of H_2SO_4 at the MT station, the concentration of H_2SO_4 is expected to be much lower than that at the UB station. First, the SO_2 concentration at measurement at Longquan Town was always below the detection limit ($\sim 0.5 \text{ ppb}$) during our observation period. In comparison, median SO_2 concentration at UB station was 0.87 ppb for all days and 0.65 ppb for NPF event days during our short-term parallel observation period. The spatial decreasing trend of SO_2 concentration from urban

Beijing to the west implies a low SO₂ concentration at the MT station, especially when the nearby anthropogenic sources are sparse (Liu ~~et al.~~, 2008; Ying, 2010; Wang, 2011; Yang-Chun et al., 2013; Wang ~~et al.~~, 2011; Ying ~~et al.~~, 2010). Second, the oxidation of SO₂ by photochemistry reactions could also be limited by the low solar radiation at the MT station as we discussed ~~above~~ in 3.1.3. Third, CS, as the main sink of H₂SO₄, was comparable at the MT station to that in the UB station ~~on NPF event days (as shown in Fig.8a).~~ Altogether, the lower production rate and the equivalent loss rate of H₂SO₄ at the MT station likely results in the lower H₂SO₄ concentration, in comparison to UB station. Due to the lack of H₂SO₄ measurement, the NPF mechanism at the MT station cannot be inferred. Nevertheless, we show that the occurrence of NPF as a response to photochemistry (and very likely to H₂SO₄) and CS in Fig. 9d. It is clear that high UV intensity and low CS favored the occurrence of NPF. However, there existed exceptions. For example, ~~it was an undefined day on June 28 despite of the high UV intensity and low CS. Besides,~~ two NPF events were observed even when the UV intensity was low and the CS was high ~~besides, it was an undefined day on June 28 despite of the high UV intensity and low CS.~~ These exceptional cases will be discussed in detail in Section 3.6.1 and 3.6.2, respectively.

3.2 NPF event start time at both stations

~~There was no significant difference in NPF event start time between the long-term and short-term parallel observations at UB site. In this section, we only compare NPF event start time of common events at UB and MT sites during the short-term parallel observations. During our observation, there was no advection of air masses between the two sites on common NPF event days, indicating that the NPF events occurred at each site independently. As shown in Table 1, all common NPF events started after sunrise and prior to noon except the two non-local NPF events at MT station. However, NPF event start time was different between the two sites. Earlier researches in Nanjing, China and Nordic stations showed the similar results that NPF events can be observed simultaneously at two or more sites, but the start time can be different, local meteorology, source strength and background aerosols could~~

drive temporal behavior of NPF events at each sites (Hussein et al., 2009;Dai et al., 2017).

3.3 Particle formation and growth rates at both stations

The particle formation rates (J_7) at the two stations during the measurements are presented in Fig.11a. J_7 observed during the short-term parallel observation (NPF2) at UB site was in the range of $3.0\text{-}10.0\text{ cm}^{-3}\text{ s}^{-1}$ with a median of $5.4\text{ cm}^{-3}\text{ s}^{-1}$, comparable with those observed in summer 2018 and 2019 (NPF1 = $2\text{-}14.0\text{ cm}^{-3}\text{ s}^{-1}$ with a median of $4.9\text{ cm}^{-3}\text{ s}^{-1}$) and significantly higher than the values in the MT station ($0.75\text{-}3.0\text{ cm}^{-3}\text{ s}^{-1}$ with a median of $0.82\text{ cm}^{-3}\text{ s}^{-1}$) for common NPF events (Fig.11b). These values are comparable to earlier observations in urban Beijing and another regional background station in North China Plain (NCP) (Wang et al., 2013). Earlier observations in NCP and Yangtze River Plain also observed higher formation rates at urban sites than corresponding background sites by roughly a factor of 2 due to lower anthropogenic emissions at background sites (Wang et al., 2013;Dai et al., 2017;Shen et al., 2018). The much lower J_7 observed at MT station is very likely associated with the low H_2SO_4 concentration at this station, as we discussed above. However, other reasons, such as the low concentration of H_2SO_4 stabilizers, e.g., amines, cannot be ruled out either. Also, the J_7 at UB station could be affected by particle emissions due to the proximity of the location to the highway (Kontkanen et al., 2020).

The particle growth rates in size range of $7\text{-}15\text{ nm}$ ($\text{GR}_{7\text{-}15\text{nm}}$) at the UB station ($4.8\text{-}12.9\text{ nm/h}$ with a median of 7.8 nm/h) during NPF2 was also comparable with the whole summers (NPF1) ($4.8\text{-}12.9\text{ nm/h}$ with a median of 8.5 nm/h). While the difference in J_7 was 7 times higher in UB than in MT, the observed GR were only a slightly higher at UB than at the MT station ($5.7\text{-}10.5\text{ nm/h}$ with a median of 6.5 nm/h) for common NPF events (Fig.11c&d), implying that precursors needed for particle formation were much more abundant in the polluted urban environment (Wang et al., 2013), while those needed for growth are rather comparable. The GR at UB station was comparable with other long-term observation at UB station ($1.1\text{-}8.0\text{ nm/h}$) in 2018, and other urban areas in China (Herrmann et al., 2014;Chu et al., 2019;Deng et al., 2020b). Consistent with earlier observations showing that H_2SO_4 could

only contribute to a small fraction of the particle growth at this size range (Paasonen et al., 2018; Qi et al., 2018; Guo et al., 2020), the growth rates at both stations cannot be explained by the H₂SO₄ concentration. This implies that other condensable species, very likely low-volatility organic vapors, play an important role in particle growth at both stations. At the UB station, anthropogenic VOCs are dominant precursors of these low-volatility organic vapors (Guo et al., 2020; Deng et al., 2020a), while VOCs at MT station, with rare anthropogenic sources, are likely dominated by biogenic emissions.

3.4 Ending diameters of newly-formed grown particles

Earlier observations have shown that diameters of newly-formed particles should be larger than 70 nm to contribute to cloud condensation nuclei significantly (Man et al., 2015; Ma et al., 2021) and will be considered as haze particles when their size reaches larger than 100 nm (Kulmala et al., 2021). In Fig. 12, we show ending diameters (End Dp) of newly formed grown particles during our observations at both sites. End Dp during the observation from June 14 to July 14 at UB site (21-105 nm, with a median of 49 nm, Fig.12a) had similar characteristics as those during the long-term observation in summer (21-126 nm, with a median of 56 nm, Fig.12a) where most of End Dp were in the range of 25-70 nm. As shown in Fig.12b, 61% of End Dp were in the range of 25-70 nm, and only 9% of End Dp were larger than 100 nm during our observation in summer 2018 and 2019 at UB site. We found that the ending diameters slightly higher at UB site than MT site, but the difference is not significant (49 nm vs 45 nm) as shown in Fig. R12c.

Earlier research has pointed out that in order to observe particle growth until 100 nm at a measurement station under typical conditions, simultaneous NPF should happen over a very large area (e.g. with wind speed 5 m/s and growth rate of 3 nm/h from the station to roughly 600 km upwind from the station) (Paasonen et al., 2018). During our observation in summer 2018 and 2019, most of the newly formed modes kept growing for about 20 hours after an NPF event started, and the maximum horizontal extension of the observed NPF events in the growth stage is restricted to within about 200 km (~2° in latitude) north of UB site (Fig. 13).

As shown in Fig.13, the population density is also higher within the area extending ~200 km north than beyond this limit. Therefore, it seems that NPF events were limited to the regions with some contribution from anthropogenic emissions during air mass transport from north to Beijing. Roughly similar extent of the NPF area is also seen in other directions. However, towards the south it is more likely that increasing condensation sink from accumulating pollution becomes the limiting factor for NPF occurrence rather than decreasing strength in emission sources. NPF events at MT station had similar characteristics as those at UB station with the NPF event region extending a few hundred kilometers towards the north. The NPF events in this direction were disrupted after a relatively similar distance (or they enter the growth stagnation phase, which will be discussed in section 3.6.3). The limited NPF event area could possibly explain why most End Dp we observed were smaller than 70 nm.

3.5 Effect of topography

In Figure 14 we show average particle number size distribution and particle number concentration on NPF event and non-event days during our short-term parallel observation at both sites. On NPF event days, nucleation and Aitken mode particle number concentrations were much smaller at MT station than those at UB station due to smaller particle formation rates and less anthropogenic emissions. Interestingly, accumulation mode particle number concentrations were higher at MT station ($701\text{-}2900\text{ cm}^{-3}$, with a median of 1500 cm^{-3}) than that at UB station ($350\text{-}1416\text{ cm}^{-3}$ with a median of 700 cm^{-3}) (Fig.14b). Due to the close proximity of the two measurement sites, the air mass arrival directions and source regions were (mostly) similar at both sites throughout the measurement period, hence the regional and transported cannot explain the higher accumulation mode particle number concentration at MT site. As there were few primary emissions at MT site, the accumulation mode particles could be attributed to secondary particles (Kulmala et al., 2021), indicating particles at MT station were more aged than those at UB station (Fig.14a). The possible reasons is that mountains block pollution diffusion, which in the end resulted in comparable CS at MT station as UB station.

Figure 15 shows an example of the wind distribution before and during NPF event on June 30, 2019 at 850 hPa (close to the altitude of MT station) and 10 m above ground level. As shown in Fig.15, the reanalyzed wind directions at 850 hPa were similar as those at 10 m above the ground level at MT station. Actually, the wind conditions on other NPF event days at MT station during our observation had similar characteristics that the wind directions were similar between 850 hPa and 10 m above ground level indicating air masses well mixed during NPF events. Earlier observations also found NPF event happened uniformly within the mixing layer at their observation stations and particle number size distribution remains roughly constant within the mixing layer (Shen et al., 2018; Lampilahti et al., 2021).

3.6 case studies

3.6.1 Non-local NPF events at ~~the~~ MT station

As we discussed above, NPF events at MT stations were favored by strong photochemistry (sufficient solar radiation) and low CS. However, we also observed two NPF events under low solar radiation and high CS on June 15 and 25. These two NPF events had similar characteristics, and we explain the case on June 15 in detail. During this case, air masses arrived at both stations from south-east around 9:00 LT as shown in Fig. 4b16b&d, resulting in high CS especially at MT ~~station~~ and UB stations (Fig. 4a16a&c). The NPF event at the UB station was observed around 11:00 LT, with a high median J_7 of $5.56 \text{ cm}^{-3}\text{s}^{-1}$, whereas no indication of NPF event at MT was observed until 15:00 likely due to the high CS. After 15:00 LT, a new growing mode from 15 nm appeared at MT station. Because there was no intense increase of sub-15 nm particle number concentration throughout the whole event, the NPF event at MT station was not local but occurred somewhere else and transported to MT station. This a common phenomenon, particularly when the conditions do not favor NPF events to occur on site, but are NPF-favorable somewhere else. The particles formed off-site are transported vertically or horizontally and observed on site (Dada et al., 2018; Leino et al., 2019). Different from other NPF events, this non-local NPF event was associated with strong southerly wind (Fig. 4e16e), the NPF event observed at the MT station might originate from

urban areas 60 km south to the station as shown in Fig.1, assuming the NPF event started around 9:00 and the mean wind speed was 3 m/s.

3.6.2 Undefined day under low CS and high UV ~~condition~~ at MT station

Interestingly, we also observed an undefined day at MT station with low CS (0.006 s^{-1}) and high UV (28 W/m^2) on June 28 (Fig. ~~9e & Fig. 12e~~17c) as there seems to be a very weak ‘banana’ around 13:00 in the particle number size distribution plot. All other days with such conditions were classified as NPF event days. In this case, the reasonable explanation would be low precursor vapours which we think are SO_2 in our case. On this day, an air mass from Inner-Mongolia arrived at both stations, resulting in very low SO_2 concentration at the UB station among all NPF event days during our observation as shown in Fig. 34. It is reasonable to assume that the SO_2 concentration was even lower at the MT station than at the UB station, and low H_2SO_4 concentration could also be expected, which could be insufficient to trigger an NPF event. This is consistent with an earlier long-term observation at Shangdianzi, another background site of Beijing, where the NPF events were suppressed by air masses from Inner-Mongolia due to the low precursor concentrations (Shen et al., 2018). In comparison, we observed a very weak NPF event at UB station at the same day, as local emissions were enough to supply enough vapors to initiate NPF event.

4—Conclusion

3.6.3 Growth stagnant and shrinkage case during our observation

During our observations in summer 2018 and 2019 at urban site and the observation from June 14 to July 14, 2019 at MT site, there were some cases where the newly-formed particles entered a phase of growth stagnation or even displayed a decreasing mode diameter. On June 30, 2019 such case occurred simultaneously at both sites and we chose this day for a case study.

As shown in Fig.18 a&b, the newly-formed particles entered a phase of growth stagnation almost at the same time around 12:00 at both sites. Particle mode diameters decreased from 31 nm to 15 nm at UB station around 15:00, under relatively calm meteorological condition indicating meteorological condition could not be the reason for particle sizes decrease on

June 30, 2019 at UB site. Around the same time, mode diameter at MT station also decreased gradually from 25 nm to 16 nm. Earlier observations in summer-time Beijing have speculated mode diameter decrease to be related to particle evaporation, which is triggered by favorable meteorological conditions and vapor dilution (Zhang et al., 2016). From Fig.13, we see, that the air masses observed during the growth stagnation or diameter decrease (both marked under growth stagnation in the figure) were often located quite far in the north over the less populated areas during the onset time of regional NPF. It is also possible, that the less favorable initial conditions for particle formation and growth over these areas, combined with increasing wind speed or temporal changes in the growth rate, could explain the observations of decreasing particle sizes without evaporation (Kivekäs et al., 2016; Hakala et al., 2019).

4 Summary and conclusions

We conducted observations of NPF events at an urban site (UB) and a background mountain site (MT) in Beijing and fully analyzed the favorable conditions for NPF event occurrences at each of the sites. In order to identify the similarities and differences between NPF events at both stations in terms of frequency, intensity and mechanisms, we compared certain NPF characteristics including particle formation rate, growth rate as well as NPF event start time and ending diameters of newly-formed growing particles at both stations. We found that NPF events are most of the time a regional phenomenon occurring over the studied areas and connected closely with air masses source regions during our observation. The air masses from north favored common NPF events more than any other mass trajectories due to their associated clean air masses and thus low CS. –Additionally, air masses from the north group always resulted in an NPF event at UB station, while other factors still suppressed their occurrence at the MT station. For example, we found that sufficiently high solar radiation, e.g. UV (UVA+UVB) intensity larger than 15 W/m² is required for an NPF event to occur at MT and NPF events observed under solar radiation conditions smaller than 15 W/m² were rather transported NPF events from areas upwind to MT station. Another factor suppressing the occurrence of NPF events at MT is the too low precursor gas concentrations (e.g. SO₂) which was visible in MT rather than at UB. Moreover, we found that the CS limit for NPF event

occurrence at UB station was $\sim 0.032 \text{ s}^{-1}$, which is consistent with earlier observations in urban Beijing. In comparison, at MT station the CS limit could be only $\sim 0.013 \text{ s}^{-1}$, above which local-NPF events could possibly be suppressed associated with the lower SO_2 concentration.

Although NPF events could happen simultaneously at both stations, the NPF event strength (particle formation rates) was significantly higher at UB than MT station, possibly due to spatial inhomogeneity in the sources of aerosol precursor compounds as well as solar radiation. In comparison, the particle growth rates in size range of 7-15 nm were ~~comparable between these two sites. This clearly suggested that particle formation and further growth are mediated by different vapors. The ending diameters of newly formed grown particles were also slightly~~ higher at UB than MT station, ~~most likely due to the more abundant precursors at the urban area. Our results suggest that. Regional~~ NPF events at urban areas ~~could have a bigger influence on global/regional climate and were observed to occur with the horizontal extent within around 200 kilometers when air pollution masses arriving at Beijing from the north, as a result, only a few NPF events were observed to end with mode diameters larger than those at clean~~ 70 nm. The size of the area with NPF events upwind our observation seems to be connected with population density that weaker NPF event was assumed to happen in less populated areas.

~~NPF events in urban areas were likely transported to regional background sites during our observation. Yet, it remains unknown whether NPF event at regional background sites can affect NPF event in urban areas despite the fact that NPF event and particle growth which are driven by regional air masses can also interact with urban climate (Salma et al., 2016, Du et al. 2021). To fill the knowledge gap, long-term~~ Overall, our results highlight the importance of anthropogenic emissions for NPF events occurrence and subsequently growth in north China plain during summer. However, there are still some uncertainties due to the limited data set. For more robust knowledge on NPF events in north China plain, long-term and more comprehensive observations on NPF events upwind and downwind urban Beijing are important. Such observations can shed light into the regionality of NPF events and the

dynamical development of the aerosol population influenced by radical chemistry in the plume of a megacity. ~~The importance of NPF events as a potential crucial contributor to haze and air pollution in general (Kulmala 2015, Kulmala et al., 2021) need be investigated in not only long-term but also more sites with comprehensive observations (Kulmala, 2018) for better implementations in global models and policy making strategies.~~

Conflict of interest: The authors declare no competing interests.

Author contributions: YZ, CY, YG, XY performed the measurements. YZ, SH, CY, YG, LD, XY analyzed the data. YZ, CY, SH, LD wrote the manuscript. All authors reviewed the paper and contributed to the scientific discussions.

Data availability: The data displayed in this manuscript will be available online at zenodo.com once the manuscript is in its final publication format.

Financial support: This publication has been produced within the framework of the EMME-CARE project, which has received funding from the European Union's Horizon 2020 Research and Innovation Programme (under grant agreement no. 856612) and the Government of Cyprus. This research has also received funding from the European Commission grant agreement no. 742206 ("ERC-ATM-GTP") as well as Academy of Finland Projects 316114 & 311932. Simo Hakala acknowledges the doctoral programme in Atmospheric Sciences (ATM-DP, University of Helsinki) for financial support. The sole responsibility of this publication lies with the author. The European Union is not responsible for any use that may be made of the information contained therein.

782

783 **5 References**

784 Cai, R., and Jiang, J.: A new balance formula to estimate new particle formation rate: reevaluating the
785 effect of coagulation scavenging, *Atmos Chem Phys*, 17, 12659-12675, 10.5194/acp-17-12659-2017,
786 2017.

787 Cai, R., Yang, D., Fu, Y., Wang, X., Li, X., Ma, Y., Hao, J., Zheng, J., and Jiang, J.: Aerosol surface
788 area concentration: a governing factor in new particle formation in Beijing, *Atmos Chem Phys*, 17,
789 12327-12340, 10.5194/acp-17-12327-2017, 2017.

790 Cai, R., Yan, C., Yang, D., Yin, R., Lu, Y., Deng, C., Fu, Y., Ruan, J., Li, X., Kontkanen, J., Zhang, Q.,
791 Kangasluoma, J., Ma, Y., Hao, J., Worsnop, D. R., Bianchi, F., Paasonen, P., Kerminen, V.-M., Liu, Y.,
792 Wang, L., Zheng, J., Kulmala, M., and Jiang, J.: Sulfuric acid-amine nucleation in urban Beijing,
793 *Atmospheric Chemistry and Physics Discussions*, 10.5194/acp-2020-1060, 2020.

794 Carnerero, C., Pérez, N., Reche, C., Ealo, M., Titos, G., Lee, H.-K., Eun, H.-R., Park, Y.-H., Dada, L.,
795 Paasonen, P., Kerminen, V.-M., Mantilla, E., Escudero, M., Gómez-Moreno, F. J., Alonso-Blanco, E.,
796 Coz, E., Saiz-Lopez, A., Temime-Roussel, B., Marchand, N., Beddows, D. C. S., Harrison, R. M.,
797 Petäjä, T., Kulmala, M., Ahn, K.-H., Alastuey, A., and Querol, X.: Vertical and horizontal distribution
798 of regional new particle formation events in Madrid, *Atmos Chem Phys*, 18, 16601-16618,
799 10.5194/acp-18-16601-2018, 2018.

800 Chu, B., Dada, L., Liu, Y., Yao, L., Wang, Y., Du, W., Cai, J., Daellenbach, K., Chen, X., Simonen, P.,
801 Zhou, Y., Deng, C., Fu, Y., Yin, R., Li, H., He, X.-C., Feng, Z., Yan, C., Kangasluoma, J., and Kulmala,
802 M.: Particle growth with photochemical age from new particle formation to haze in the winter of
803 Beijing, China, *Science of The Total Environment*, 753, 10.1016/j.scitotenv.2020.142207, 2021.

804 Chu, B. W., Kerminen, V. M., Bianchi, F., Yan, C., Petäjä, T., and Kulmala, M.: Atmospheric new
805 particle formation in China, *Atmos Chem Phys*, 19, 115-138, <https://doi.org/10.5194/acp-19-115-2019>,
806 2019.

807 Dada, L., Paasonen, P., Nieminen, T., Buenrostro Mazon, S., Kontkanen, J., Peräkylä, O., Lehtipalo,
808 K., Hussein, T., Petäjä, T., Kerminen, V.-M., Bäck, J., and Kulmala, M.: Long-term analysis of
809 clear-sky new particle formation events and nonevents in Hyytiälä, *Atmos Chem Phys*, 17, 6227-6241,

10.5194/acp-17-6227-2017, 2017.

Dada, L., Chellapermal, R., Buenrostro Mazon, S., Paasonen, P., Lampilahti, J., Manninen, H. E., Junninen, H., Petäjä, T., Kerminen, V.-M., and Kulmala, M.: Refined classification and characterization of atmospheric new-particle formation events using air ions, *Atmos Chem Phys*, 18, 17883-17893, 10.5194/acp-18-17883-2018, 2018.

Dada, L., Lehtipalo, K., Kontkanen, J., Nieminen, T., Baalbaki, R., Ahonen, L., Duplissy, J., Yan, C., Chu, B., Petäjä, T., Lehtinen, K., Kerminen, V.-M., Kulmala, M., and Kangasluoma, J.: Formation and growth of sub-3-nm aerosol particles in experimental chambers, *Nat Protoc*, , 15, 1013-1040, 10.1038/s41596-019-0274-z, 2020a.

Dada, L., Ylivinkka, I., Baalbaki, R., Li, C., Guo, Y., Yan, C., Yao, L., Sarnela, N., Jokinen, T., Daellenbach, K. R., Yin, R., Deng, C., Chu, B., Nieminen, T., Kontkanen, J., Stolzenburg, D., Sipilä, M., Hussein, T., Paasonen, P., Bianchi, F., Salma, I., Weidinger, T., Pikridas, M., Sciare, J., Jiang, J., Liu, Y., Petäjä, T., Kerminen, V.-M., and Kulmala, M.: Sources and sinks driving sulphuric acid concentrations in contrasting environments: implications on proxy calculations, *Atmos. Chem. Phys. Discuss.*, 10.5194/acp-2020-155, 2020b.

Dai, L., Wang, H., Zhou, L., An, J., Tang, L., Lu, C., Yan, W., Liu, R., Kong, S., Chen, M., Lee, S., and Yu, H.: Regional and local new particle formation events observed in the Yangtze River Delta region, China, *Journal of Geophysical Research: Atmospheres*, 122, 2389-2402, 10.1002/2016jd026030, 2017.

Dal Maso, M., Kulmala, M., Riipinen, I., Wagner, R., Hussein, T., Aalto, P. P., and Lehtinen, K. E. J.: Formation and growth of fresh atmospheric aerosols: eight years of aerosol size distribution data from SMEAR II, Hyytiälä, Finland, *Boreal Environ Res*, 10, 323-336, 2005.

Deng, C., Cai, R., Yan, C., Zheng, J., and Jiang, J.: Formation and growth of sub-3 nm particles in megacities: impact of background aerosols, *Faraday Discuss*, 10.1039/d0fd00083c, 2020a.

Deng, C., Fu, Y., Dada, L., Yan, C., Cai, R., Yang, D., Zhou, Y., Yin, R., Lu, Y., Li, X., Qiao, X., Fan, X., Nie, W., Kontkanen, J., Kangasluoma, J., Chu, B., Ding, A., Kerminen, V. M., Paasonen, P., Worsnop, D. R., Bianchi, F., Liu, Y., Zheng, J., Wang, L., Kulmala, M., and Jiang, J.: Seasonal Characteristics of New Particle Formation and Growth in Urban Beijing, *Environ Sci Technol*, 54,

8547-8557, 10.1021/acs.est.0c00808, 2020b.

Du, W., Dada, L., Zhao, J., Chen, X., Daellenbach, K. R., Xie, C., Wang, W., He, Y., Cai, J., Yao, L., Zhang, Y., Wang, Q., Xu, W., Wang, Y., Tang, G., Cheng, X., Kokkonen, T. V., Zhou, W., Yan, C., Chu, B., Zha, Q., Hakala, S., Kurppa, M., Järvi, L., Liu, Y., Li, Z., Ge, M., Fu, P., Nie, W., Bianchi, F., Petäjä, T., Paasonen, P., Wang, Z., Worsnop, D. R., Kerminen, V.-M., Kulmala, M., and Sun, Y.: A 3D study on the amplification of regional haze and particle growth by local emissions, *npj Climate and Atmospheric Science*, 4, 10.1038/s41612-020-00156-5, 2021.

Ehn, M., Thornton, J.A., Kleist, E., Sipila, M., Junninen, H., Pullinen, I., Springer, M., Rubach, F., Tillmann, R., Lee, B., Lopez-Hilfiker, F., Andres, S., Acir, I.-H., Rissanen, M., Jokinen, T., Schobesberger, S., Kangasluoma, J., Kontkanen, J., Nieminen, T., Kurten, T., Nielsen, L. B., Jorgensen, S., Kjaergaard, H. G., Canagaratna, M., Maso, M. D., Berndt, T., Petaja, T., Wahner, A., Kerminen, V.-M., Kulmala, M., Worsnop, D. R., Wildt, J., and Mentel, T. F.: A large source of low-volatility secondary organic aerosol, *Nature*, 506, 476–479., 2014.

Gao, Y., Zhang, D., Wang, J., Gao, H., and Yao, X.: Variations in Ncn and Nccn over China marginal seas related to marine traffic emissions, new particle formation and aerosol aging, *Atmos. Chem. Phys.*, in press 2020.

Guo, S., Hu, M., Zamora, M. L., Peng, J. F., Shang, D. J., Zheng, J., Du, Z. F., Wu, Z., Shao, M., Zeng, L. M., Molina, M. J., and Zhang, R. Y.: Elucidating severe urban haze formation in China, *P Natl Acad Sci USA*, 111, 17373-17378, 10.1073/pnas.1419604111, 2014.

Guo, S., Hu, M., Peng, J., Wu, Z., Zamora, M. L., Shang, D., Du, Z., Zheng, J., Fang, X., Tang, R., Wu, Y., Zeng, L., Shuai, S., Zhang, W., Wang, Y., Ji, Y., Li, Y., Zhang, A. L., Wang, W., Zhang, F., Zhao, J., Gong, X., Wang, C., Molina, M. J., and Zhang, R.: Remarkable nucleation and growth of ultrafine particles from vehicular exhaust, *Proc Natl Acad Sci U S A*, 117, 3427-3432, 10.1073/pnas.1916366117, 2020.

Hakala, S., Alghamdi, M. A., Paasonen, P., Vakkari, V., Khoder, M. I., Neitola, K., Dada, L., Abdelmaksoud, A. S., Al-Jeelani, H., Shabbaj, I. I., Almeahmadi, F. M., Sundström, A.-M., Lihavainen, H., Kerminen, V.-M., Kontkanen, J., Kulmala, M., Hussein, T., and Hyvärinen, A.-P.: New particle formation, growth and apparent shrinkage at a rural background site in western Saudi Arabia, *Atmos*

866 Chem Phys, 19, 19, <https://doi.org/10.5194/acp-19-10537-2019>, 2019.

867 Hamed, A., Korhonen, H., Sihto, S.-L., Joutsensaari, J., Järvinen, H., Petäjä, T., Arnold, F., Nieminen,
868 T., Kulmala, M., Smith, J. N., Lehtinen, K. E. J., Laaksonen, A., and High relative humidity suppresses
869 continental new particle formation events, 2010.

870 Hamed, A., Korhonen, H., Sihto, S.-L., Joutsensaari, J., Järvinen, H., Petäjä, T., Arnold, F., Nieminen,
871 T., Kulmala, M., Smith, J. N., Lehtinen, K. E. J., and Laaksonen, A.: The role of relative humidity in
872 continental new particle formation, *Journal of Geophysical Research*, 116, 10.1029/2010jd014186,
873 2011.

874 Herrmann, E., Ding, A. J., Kerminen, V. M., Petäjä, T., Yang, X. Q., Sun, J. N., Qi, X. M., Manninen,
875 H., Hakala, J., Nieminen, T., Aalto, P. P., Kulmala, M., and Fu, C. B.: Aerosols and nucleation in
876 eastern China: first insights from the new SORPES-NJU station, *Atmos Chem Phys*, 14, 2169-2183,
877 10.5194/acp-14-2169-2014, 2014.

878 Hussein, T., Junninen, H., Tunved, P., Kristensson, A., Dal Maso, M., Riipinen, I., Aalto, P. P.,
879 Hansson, H. C., Swietlicki, E., and Kulmala, M.: Time span and spatial scale of regional new particle
880 formation events over Finland and Southern Sweden, *Atmos Chem Phys*, 9, 4699-4716,
881 10.5194/acp-9-4699-2009, 2009.

882 Jun, Y.-S., Jeong, C.-H., Sabaliauskas, K., Richard Leitch, W., and Evans, G. J.: A year-long
883 comparison of particle formation events at paired urban and rural locations, *Atmospheric Pollution*
884 *Research*, 5, 447-454, 10.5094/apr.2014.052, 2014.

885 Kangasluoma, J., Cai, R., Jiang, J., Deng, C., Stolzenburg, D., Ahonen, L. R., Chan, T., Fu, Y., Kim,
886 C., Laurila, T. M., Zhou, Y., Dada, L., Sulo, J., Flagan, R. C., Kulmala, M., Petäjä, T., and Lehtipalo,
887 K.: Overview of measurements and current instrumentation for 1–10 nm aerosol particle number size
888 distributions, *J Aerosol Sci*, 148, 10.1016/j.jaerosci.2020.105584, 2020.

889 Kerminen, V. M., Chen, X. M., Vakkari, V., Petäjä, T., Kulmala, M., and Bianchi, F.: Atmospheric new
890 particle formation and growth: review of field observations, *Environ Res Lett*, 13,
891 <https://doi.org/10.1088/1748-9326/aadf3c>, 2018.

892 Komppula, M., Sihto, S.-L., Korhonen, H., Lihavainen, H., Kerminen, V.-M., Kulmala, M., and
893 Viisanen, Y.: New particle formation in air mass transported between two measurement sites in

894 Northern Finland, *Atmos Chem Phys*, 6, 14, www.atmos-chem-phys.net/6/2811/2006/, 2006.

895 Kontkanen, J., Deng, C., and Fu, Y., Dada, L., Zhou, Y., Cai, J., Daellenbach, R.-K., Hakala, S.,
896 Kokkonen, V.-T., Lin, Z., Liu, Y., Wang, Y., Yan, C., Petäjä, T., Jiang, J., Kulmala, M and Paasonen, P.:
897 Size-resolved particle number emissions in Beijing determined from measured particle size
898 distributions, *Atmos Chem Phys*, 20, 11329–11348, <https://doi.org/10.5194/acp-20-11329-2020>, 2020.

899 Kivekäs, N., Carpmann, J., Roldin, P., Leppä, J., O’Connor, E., Kristensson, A., and Asmi, E.:
900 Coupling an aerosol box model with one-dimensional flow: a tool for understanding
901 observations of new particle formation events, *Tellus B*, 68, 29706,
902 [doi:10.3402/tellusb.v68.29706](https://doi.org/10.3402/tellusb.v68.29706), 2016.

903 Kristensson, A., Johansson, M., Swietlicki, E., Kivekäs, N., Hussein, T., Nieminen, T., Kulmala, M.,
904 and Dal Maso, M.: NanoMap: geographical mapping of atmospheric new particle formation through
905 analysis of particle number size distribution data, *Boreal Environ. Res.*, 19 (suppl. B), 329–342,
906 2014.

907 Kulmala, M., Petäjä, T., Nieminen, T., Sipilä, M., Manninen, H. E., Lehtipalo, K., Dal Maso, M.,
908 Aalto, P. P., Junninen, H., Paasonen, P., Riipinen, I., Lehtinen, K. E. J., Laaksonen, A., and Kerminen,
909 V. M.: Measurement of the nucleation of atmospheric aerosol particles, *Nat Protoc*, 7, 1651-1667,
910 <https://doi.org/10.1038/nprot.2012.091>, 2012.

911 Kulmala, M., Dada, L., Dällenbach, K., Yan, C., Stolzenburg, D., Kontkanen, J., Ezhova, E., Hakala,
912 S., Tuovinen, S., Kokkonen, T., Kurppa, M., Cai, R., Zhou, Y., Yin, R., Baalbaki, R., Chan, T., Chu, B.,
913 Deng, C., Fu, Y., Ge, M., He, H., Heikkinen, L., Junninen, H., Nei, W., Rusanen, A., Vakkari, V.,
914 Wang, Y., Wang, L., yao, I., Zheng, J., Kujansuu, J., Kangasluoma, J., Petäjä, T., Paasonen, P., Järvi,
915 L., Worsnop, D., Ding, A., Liu, Y., Jiang, J., Bianchi, F., Yang, G., Liu, Y., Lu, Y., and Kerminen,
916 V.-M.: Is reducing new particle formation a plausible solution to mitigate particulate air pollution in
917 Beijing and other Chinese megacities?, *Faraday Discuss*, 10.1039/d0fd00078g, 2021.

918 Lampilahti, J., Manninen, H. E., Nieminen, T., Mirme, S., Ehn, M., Pullinen, I., Leino, K.,
919 Schobesberger, S., Kangasluoma, J., Kontkanen, J., Järvinen, E., Väänänen, R., Yli-Juuti, T., Krejci,
920 R., Lehtipalo, K., Levula, J., Mirme, A., Decesari, S., Tillmann, R., Worsnop, D. R., Rohrer, F.,
921 Kiendler-Scharr, A., Petäjä, T., Kerminen, V.-M., Mentel, T. F., and Kulmala, M.: Zeppelin-led study

922 on the onset of new particle formation in the planetary boundary layer, *Atmospheric Chemistry and*
923 *Physics Discussions*, 10.5194/acp-2021-282, 2021.

924 Lehtipalo, K., Leppä, J., Kontkanen, J., Kangasluoma, J., Wimmer, D., Franchin, A., Schobesberger,
925 S., Junninen, H., Petäjä, T., Sipilä, M., Mikkilä, J., Vanhanen, J., Worsnop, D. r., and Kulmala, M.:
926 methods for determining particle size distribution and growth rates between 1 and 3 nm using the
927 Particle Size Magnifier, *Boreal Environ Res*, 19 215-236, 2014.

928 Lehtipalo, K., Yan, C., Dada, L., Bianchi, F., Xiao, M., Wagner, R., Stolzenburg, D., Ahonen, L. R.,
929 Amorim, A., Baccarini, A., Bauer, P. S., Baumgartner, B., Bergen, A., Bernhammer, A. K.,
930 Breitenlechner, M., Brilke, S., Buchholz, A., Mazon, S. B., Chen, D. X., Chen, X. M., Dias, A.,
931 Dommen, J., Draper, D. C., Duplissy, J., Ehn, M., Finkenzeller, H., Fischer, L., Frege, C., Fuchs, C.,
932 Garmash, O., Gordon, H., Hakala, J., He, X. C., Heikkinen, L., Heinritzi, M., Helm, J. C., Hofbauer,
933 V., Hoyle, C. R., Jokinen, T., Kangasluoma, J., Kerminen, V. M., Kim, C., Kirkby, J., Kontkanen, J.,
934 Kurten, A., Lawler, M. J., Mai, H. J., Mathot, S., Mauldin, R. L., Molteni, U., Nichman, L., Nie, W.,
935 Nieminen, T., Ojdanic, A., Onnela, A., Passananti, M., Petäjä, T., Piel, F., Pospisilova, V., Quéléver, L.
936 L. J., Rissanen, M. P., Rose, C., Sarnela, N., Schallhart, S., Schuchmann, S., Sengupta, K., Simon, M.,
937 Sipilä, M., Tauber, C., Tomé, A., Tröstl, J., Väisänen, O., Vogel, A. L., Volkamer, R., Wagner, A. C.,
938 Wang, M. Y., Weitz, L., Wimmer, D., Ye, P. L., Ylisirnio, A., Zha, Q. Z., Carslaw, K. S., Curtius, J.,
939 Donahue, N. M., Flagan, R. C., Hansel, A., Riipinen, I., Virtanen, A., Winkler, P. M., Baltensperger,
940 U., Kulmala, M., and Worsnop, D. R.: Multicomponent new particle formation from sulfuric acid,
941 ammonia, and biogenic vapors, *Sci Adv*, 4, <https://doi.org/10.1126/sciadv.aau5363>, 2018.

942 Leino, K., Lampilahti, J., Poutanen, P., Väänänen, R., Manninen, A., Buenrostro Mazon, S., Dada, L.,
943 Franck, A., Wimmer, D., Aalto, P. P., Ahonen, L. R., Enroth, J., Kangasluoma, J., Keronen, P.,
944 Korhonen, F., Laakso, H., Matilainen, T., Siivola, E., Manninen, H. E., Lehtipalo, K., Kerminen,
945 V.-M., Petäjä, T., and Kulmala, M.: Vertical profiles of sub-3 nm particles over the boreal
946 forest, *Atmos Chem Phys*, 19, 4127-4138, 10.5194/acp-19-4127-2019, 2019.

947 Liu, J., Zhang, X. L., Xu, X. F., and Xu, H. H.: Comparison analysis of variation characteristics of
948 SO₂, NO_x, O₃ and PM_{2.5} between rural and urban areas, *Beijing Huan jing ke xue= Huanjing kexue*
949 / [bian ji, Zhongguo ke xue yuan huan jing ke xue wei yuan hui "Huan jing ke xue" bian ji wei yuan

hui.], 29, 1059-1065, 2008.

Liu, J. Q., Jiang, J. K., Zhang, Q., Deng, J. G., and Hao, J. M.: A spectrometer for measuring particle size distributions in the range of 3 nm to 10 μ m, *Front Env Sci Eng*, 10, 63-72, <https://doi.org/10.1007/s11783-014-0754-x>, 2016.

Lee, B. P., Li, Y. J., Flagan, R. C., Lo, C., and Chan, C. K.: Sizing characterization of the fast mobility particle sizer (FMPS) against SMPS and HR-ToF-AMS, *Aerosol Sci. Technol.*, 47, 1030–1037, <https://doi.org/10.1080/02786826.2013.810809>, 2013.

Lu, Y., Yan, C., Fu, Y., Chen, Y., Liu, Y., Yang, G., , Wang, Y., Bianchi, F., Chu, B., and Zhou, Y.: A proxy for atmospheric daytime gaseous sulfuric acid concentration in urban Beijing, *Atmos Chem Phys*, 19, 1971-1983, 10.5194/acp-19-1971-2019, 2019.

Ma, L., Zhu, Y., Zheng, M., Sun, Y., Huang, L., Liu, X., Gao, Y., Shen, Y., Gao, H., and Yao, X.: Investigating three patterns of new particles growing to the size of cloud condensation nuclei in Beijing's urban atmosphere, *Atmos Chem Phys*, 21, 183-200, 10.5194/acp-21-183-2021, 2021.

Man, H. Y., Zhu, Y. J., Ji, F., Yao, X. H., Lau, N. T., Li, Y. J., Lee, B. P., and Chan, C. K.: Comparison of Daytime and Nighttime New Particle Growth at the HKUST Supersite in Hong Kong, *Environ Sci Technol*, 49, 7170-7178, 2015.

Olauson, J.: ERA5: The new champion of wind power modelling?, *Renewable Energy*, 126, 322-331, 2018.

Paasonen, P., Peltola, M., Kontkanen, J., Junninen, H., Kerminen, V.-M., and Kulmala, M.: Comprehensive analysis of particle growth rates from nucleation mode to cloud condensation nuclei in boreal forest, *Atmos Chem Phys*, 18, 12085-12103, 10.5194/acp-18-12085-2018, 2018.

Pierce, J. R., and Adams P. J.: Uncertainty in global CCN concentrations from uncertain aerosol nucleation and primary emission rates. *Atmos. Chem. Phys.*, 9, 1339–1356, 10.5194/acp-9-1339-2009, 2009.

Qi, X., Ding, A., Roldin, P., Xu, Z., Zhou, P., Sarnela, N., Nie, W., Huang, X., Rusanen, A., Ehn, M., Rissanen, M. P., Petäjä, T., Kulmala, M., and Boy, M.: Modelling studies of HOMs and their contributions to new particle formation and growth: comparison of boreal forest in Finland and a polluted environment in China, *Atmos Chem Phys*, 18, 11779-11791, 10.5194/acp-18-11779-2018,

978 2018.
 979 Qi, X. M. D., A. J., Nie, W., Petaja, T., Kerminen, V. M., Herrmann, E., Xie, Y. N., Zheng, L. F.,
 980 Manninen, H., Aalto, P., Sun, J. N., Xu, Z. N., Chi, X. G., Huang, X., Boy, M., Virkkula, A., Yang, X.
 981 Q., Fu, C. B., and Kulmala, M.: Aerosol size distribution and new particle formation in the western
 982 Yangtze River Delta of China: 2 years of measurements at the SORPES station, *Atmos Chem Phys*, 15,
 983 12445-12464, 2015.
 984 Salma, I., Borsós, T., Weidinger, T., Aalto, P., Hussein, T., Dal Maso, M., and Kulmala, M.:
 985 Production, growth and properties of ultrafine atmospheric aerosol particles in an urban environment.
 986 *Atmospheric Chemistry and Physics*. 11. 10.5194/acp-11-1339-2011,2011.
 987 Salma, I., Németh, Z., Kerminen, V.-M., Aalto, P., Nieminen, T., Weidinger, T., Molnár, Á., Imre, K.,
 988 and Kulmala, M.: Regional effect on urban atmospheric nucleation, *Atmos Chem Phys*, 16,
 989 8715-8728, 10.5194/acp-16-8715-2016, 2016.
 990 Shen, X., Sun, J., Kivekäs, N., Kristensson, A., Zhang, X., Zhang, Y., Zhang, L., Fan, R., Qi, X., Ma,
 991 Q., and Zhou, H.: Spatial distribution and occurrence probability of regional new particle formation
 992 events in eastern China, *Atmos Chem Phys*, 18, 587-599, 10.5194/acp-18-587-2018, 2018.
 993 Shen, X. J., Sun, J. Y., Zhang, Y. M., Wehner, B., Nowak, A., Tuch, T., Zhang, X. C., Wang, T. T.,
 994 Zhou, H. G., Zhang, X. L., Dong, F., Birmili, W., and Wiedensohler, A.: First long-term study of
 995 particle number size distributions and new particle formation events of regional aerosol in the North
 996 China Plain, *Atmos Chem Phys*, 11, 1565-1580, 2011.
 997 Stohl, A., Forster, C., Frank, A., Seibert, P., and Wotawa, G.: Technical note: The Lagrangian particle
 998 dispersion model FLEXPART version 6.2. , *Atmospheric Chemistry and Physics*, 5, 24,
 999 10.5194/acp-5-2461-2005., 2005.
 1000 Vana, M., Komsaare, K., Hörrak, U., Mirme, S., Nieminen, T., Petäjä, T., Noe, S. M., Kontkanen, J.,
 1001 Manninen, H. E., , and Kulmala, M.: Characteristics of new-particle formation at three SMEAR
 1002 stations, *Boreal Environ Res*, 21, 17, 2016.
 1003 Wang, J., Shen, Y., Li, K., Gao, Y., Gao, H., and Yao, X.: Nucleation-mode particle pool and large
 1004 increases in Ncn and Nccn observed over the northwestern Pacific Ocean in the spring of 2014. ,
 1005 *Atmos. Chem. Phys.*, 19, 17, <https://doi.org/10.5194/acp-19-8845-2019>, 2019.

1006 Wang, M., Zhu, T., Zhang, J. P., Zhang, Q. H., Lin, W. W., Li, Y., and Wang, Z. F.: Using a mobile
1007 laboratory to characterize the distribution and transport of sulfur dioxide in and around Beijing, *Atmos*
1008 *Chem Phys*, 11, 11631-11645, 2011.

1009 Wang, Z. B., Hu, M., Sun, J. Y., Wu, Z. J., Yue, D. L., Shen, X. J., Zhang, Y. M., Pei, X. Y., Cheng, Y.
1010 F., and Wiedensohler, A.: Characteristics of regional new particle formation in urban and regional
1011 background environments in the North China Plain, *Atmos Chem Phys*, 13, 12495-12506,
1012 10.5194/acp-13-12495-2013, 2013.

1013 Wang, Z. B., Wu, Z. J., Yue, D. L., Shang, D. J., Guo, S., Sun, J. Y., Ding, A. J., Wang, L., Jiang, J. K.,
1014 Guo, H., Gao, J., Cheung, H. C., Morawska, L., Keywood, M., and Hu, M.: New particle formation in
1015 China: Current knowledge and further directions, *Science of the Total Environment*, 577, 258-266,
1016 2017.

1017 Wu, Z., Hu, M., Liu, S., Wehner, B., Bauer, S., Maßling, A., Wiedensohler, A., Petäjä, T., Dal Maso,
1018 M., and Kulmala, M.: New particle formation in Beijing, China: Statistical analysis of a 1-year data
1019 set, *Journal of Geophysical Research*, 112, 10.1029/2006jd007406, 2007.

1020 Yang-Chun, Y., Bo, H., and Wang, Y.: Changing Characteristics of the Main Air Pollutants of the
1021 Dongling Mountain in Beijing, *Environmental Science*, 34, 8, 2013.

1022 Yao, L., Garmash, O., Bianchi, F., Zheng, J., Yan, C., Kontkanen, J., Junninen, H., Mazon, S. B., Ehn,
1023 M., Paasonen, P., Sipilä, M., Wang, M. Y., Wang, X. K., Xiao, S., Chen, H. F., Lu, Y. Q., Zhang, B. W.,
1024 Wang, D. F., Fu, Q. Y., Geng, F. H., Li, L., Wang, H. L., Qiao, L. P., Yang, X., Chen, J. M., Kerminen,
1025 V. M., Petäjä, T., Worsnop, D. R., Kulmala, M., and Wang, L.: Atmospheric new particle formation
1026 from sulfuric acid and amines in a Chinese megacity, *Science*, 361, 278-281,
1027 <https://doi.org/10.1126/science.aao4839>, 2018.

1028 Yao, L., Fan, X., Yan, C., Kurtén, T., Daellenbach, K. R., Li, C., Wang, Y., Guo, Y., Dada, L., and
1029 Rissanen, M. P., Cai, J., Tham, Y. J., Zha, Q., Zhang, S., Du, W., Yu, M., Zheng, F., Zhou, Y.,
1030 Kontkanen, J., Chan, T., Shen, J., Kujansuu, J. T., Kangasluoma, J., Jiang, J., Wang, L., Worsnop, D.
1031 R., Petäjä, T., Kerminen, V.-M., Liu, Y., Chu, B., He, H., Kulmala, M., and Bianchi, F.:
1032 Unprecedented Ambient Sulfur Trioxide (SO₃) Detection: Possible Formation Mechanism and
1033 Atmospheric Implications, *Environ Sci Tech Let* 7, 809-818, 10.1021/acs.estlett.0c00615, 2020.

1034 Ying, G., Ma, J., and Xing, Y.: Comparison of air quality management strategies of PM₁₀, SO₂, and
 1035 NO_x by an industrial source complex model in Beijing, *Environmental Progress*, 26, 33-42, 2010.

1036 Yu, F. and Luo, G.: Simulation of particle size distribution with a global aerosol model:
 1037 contribution of nucleation to aerosol and CCN number concentrations, *Atmos. Chem. Phys.*,
 1038 9, 7691–7710, 10.5194/acp-9-7691-2009, 2009.

1039 Zhang, J., Chen, Z., Lu, Y., Gui, H., Liu, J., Wang, J., Yu, T., and Cheng, Y.: Observations of New
 1040 Particle Formation, Subsequent Growth and Shrinkage during Summertime in Beijing, *Aerosol Air*
 1041 *Qual Res*, 16, 1591-1602, 10.4209/aaqr.2015.07.0480, 2016.

1042 Zhou, Y., Dada, L., Liu, Y., and Fu, Y., Kangasluoma, J., Chan, T., Yan, C., Chu, B., Daellenbach, K.
 1043 R., Bianchi, F., Kokkonen, T. V., Liu, Y., Kujansuu, J., Kerminen, V.-M., Petäjä, T., Wang, L., Jiang, J.,
 1044 and Kulmala, M.: Variation of size-segregated particle number concentrations in wintertime Beijing,
 1045 *Atmos Chem Phys*, 20, 1201-1216 10.5194/acp-20-1201-2020, 2020.

1046 Zimmerman, N., Jeong, C.-H., Wang, J. M., Ramos, M., Wallace, J. S., and Evans, G. J.: A
 1047 source-independent empirical correction procedure for the fast mobility and engine exhaust particle
 1048 sizers, *Atmos. Environ.*, 100, 7, 838 10.1016/j.atmosenv.2014.10.054, 2015., 2015.

1049

1050

1051

1052 **Tables and Figures**

1053 **Table 1:** NPF event and non- event days during our observation at both stations.

Date	Type	Air masses (9:00-15:00)		GR _{7-15nm} (nm/h)		J_7 (cm ⁻³ s ⁻¹)		Event Start (LT)		Ending diameter (nm)	
		UB	MT	UB	MT	UB	MT	UB	MT	UB	MT
2019/06/14	a	North	North	8.61	-	4.97	-	9:00	8:00	71	-
2019/06/15*	a	Local	Local	12.63	-	5.56	-	11:00	15:00	82	60
2019/06/17	d	East	Local								
2019/06/18	c	Local	West		10.5		0.17		12:00		45
2019/06/19	d	South	Local								
2019/06/21	d	East	Local								
2019/06/23	e	East	East								
2019/06/24	f	Local	Local		8.21		-		12:00		50
2019/06/25*	a	Local	Local	-	-	-	-	12:00	15:00	-	53
2019/06/28	g	West	West	-		-		11:00			
2019/06/29	a	North	North	12.93	7.14	6.93	2.28	9:00	8:00	21	19
2019/06/30	a	North	North	4.82	6.57	9.86	1.37	6:30	9:30	31	25
2019/07/01	a	North	North	7.31	5.82	3.84	0.82	9:00	8:30	105	102
2019/07/02	d	Local	West								
2019/07/03	a	North	North	7.89	6.52	3.25	0.75	9:00	8:00	72	46
2019/07/04	b	Local	Local	-		-		10:00		53	
2019/07/06	a	North	North	7.39	6.51	9.21	1.75	7:00	9:30	25	19
2019/07/07	b	North	North	7.61		3.61		9:00		32	
2019/07/08	d	East	East								
2019/07/09	d	East	East								
2019/07/10	h	East	East								
2019/07/11	d	East	East								

2019/07/12	f	East	East		5.57		0.37		9:30		24
2019/07/13	c	Local	North		6.32		0.70		10:00		30
2019/07/14	a	North	North	12.04	9.86	3.91	0.89	9:30	9:30	63	47

1054 'a' means NPF event observed at both stations, 'b' means NPF event day at UB station while
 1055 non-event day at MT station, 'c' means NPF event day at MT station while non-event day at UB
 1056 station, 'd' means non-event day at both stations on the same day, 'e' means undefined day at both
 1057 stations, 'f' means undefined day at UB station while NPF event day at MT station, g means
 1058 undefined day at MT station while NPF event day at UB station, h means undefined day at UB station
 1059 while non-event day at MT station, * means NPF event observed at MT station was transported from
 1060 somewhere else. – means the values cannot be reliably calculated. Only days when particle number
 1061 size distribution were valid are included in this table.

1062

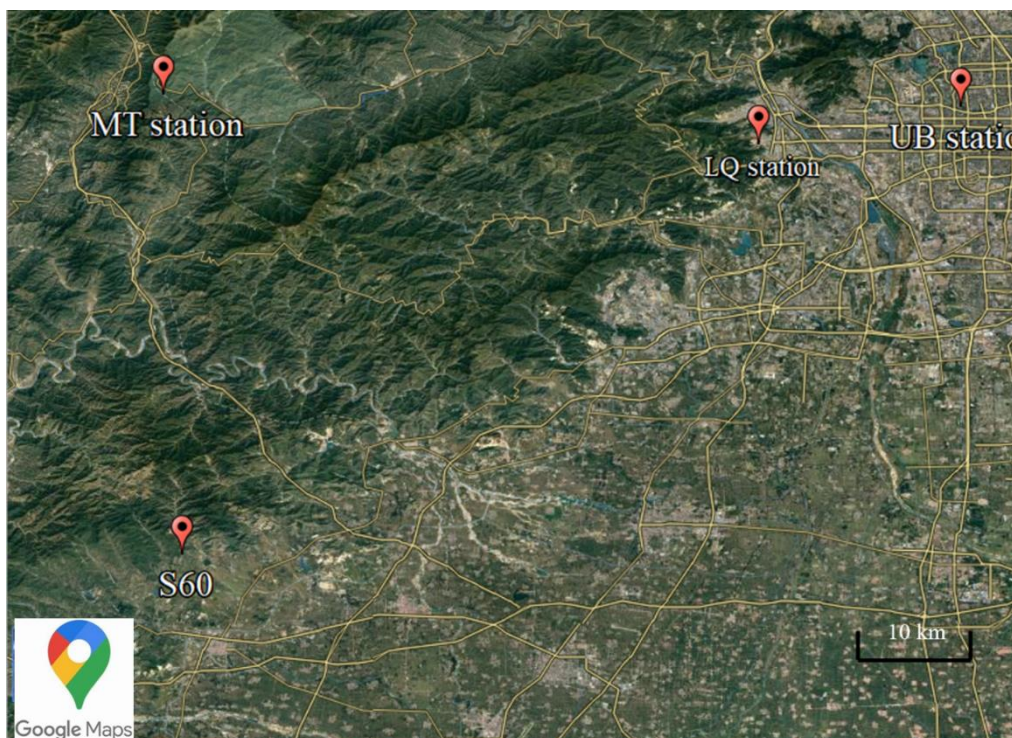


Figure 1: Map showing locations of urban station (UB), Longquan station (LQ), mountain station (MT) and another site 60 km south from MT station (S60). The S60 referred to the location where particles formed during the non-local NPF event observed at MT station on June 15, 2019. Image is produced using © Google Maps.

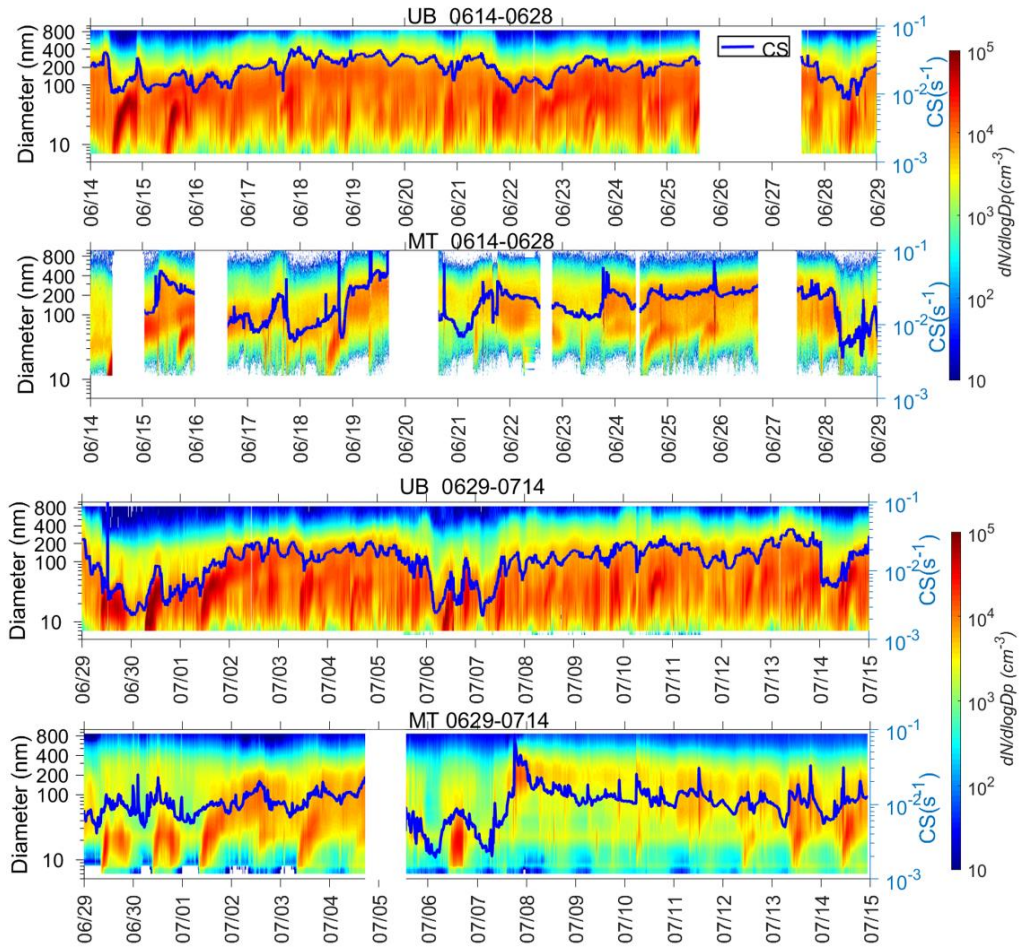


Figure 2: Time series of particle number size distribution and CS (the blue line) at UB and MT stations during our observations. Time resolutions for particle number size distribution data and CS were 8 min at UB station and 4 min at MT station, respectively.

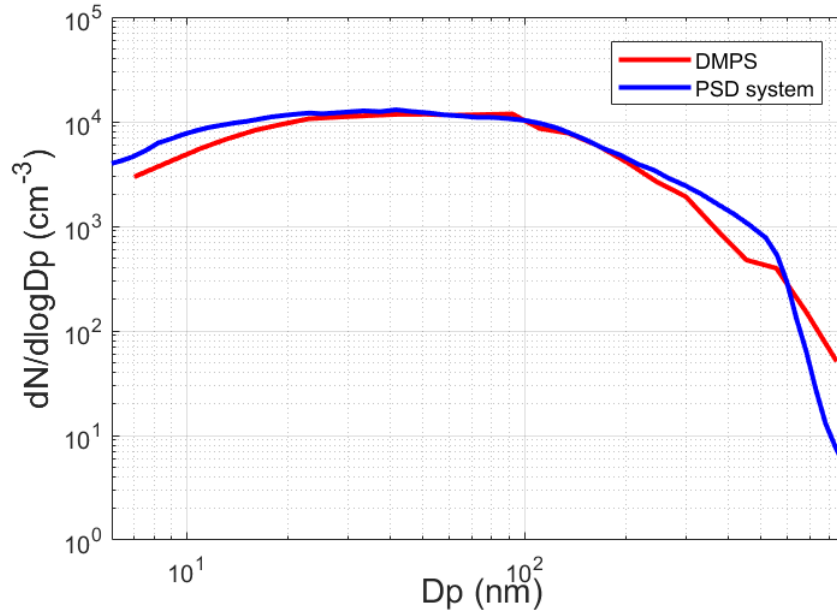


Figure 3: Median particle number size distribution in 5-900 nm measured by DMPS and PSD during our observation from June 1 to August 31, 2019 at UB station. The time window of the data is from 9:00-15:00 of every day.

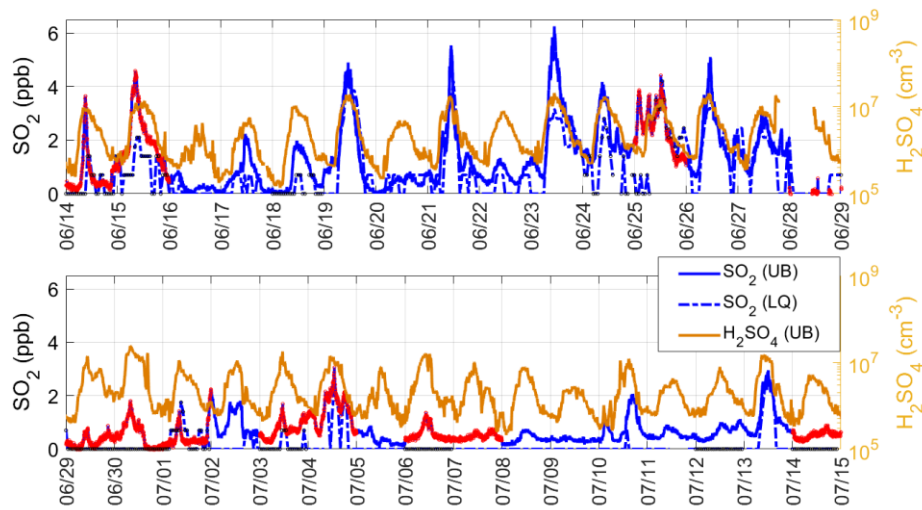


Figure 34: Time series of SO_2 concentration (ppb) at UB station and Longquan station (LQ) during our observation (left axis) as well as H_2SO_4 concentration measured at UB station (right axis). Data under detection limit are set as zero at both stations. Data on NPF event days were marked in red at UB station and black at MT station. Time resolution for SO_2 data was 5 min at UB station and 1h at LQ station, respectively.

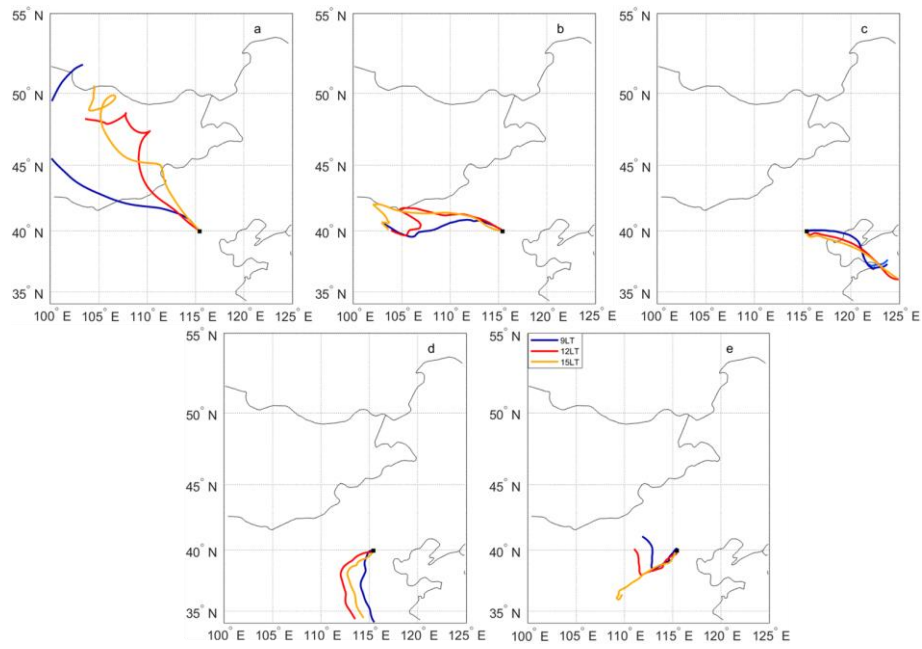


Figure 45: Examples of air masses arrived at both stations from (a) North group, (b) West group, (c) East group, (d) South group and (e) Local group during 9:00-15:00 (local time, LT). Both stations are under the same marker.

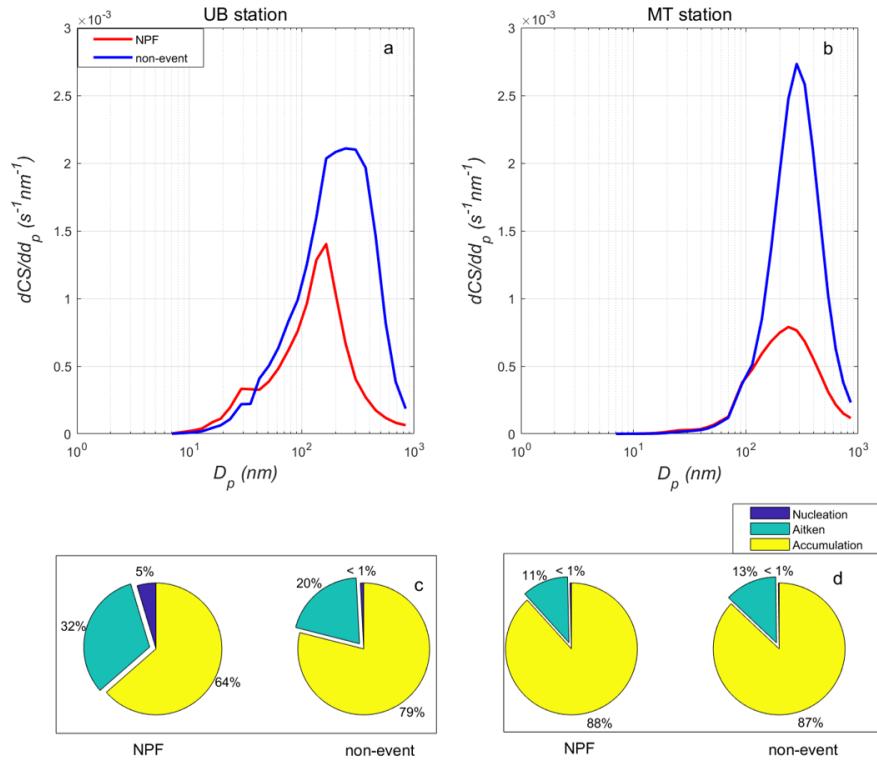


Figure 56: Median CS size distribution at UB (a) and MT (b) stations on NPF event and non-event days, respectively during 9:00-15:00 (local time, LT) and median contribution of nucleation, Aitken and accumulation mode particles to total CS at UB (c) and MT (d) stations on NPF event and non-event days, respectively during 9:00-15:00 (local time, LT). The time resolutions for CS and particle number concentration data were 8 min at UB station and 4 min at MT station, respectively.

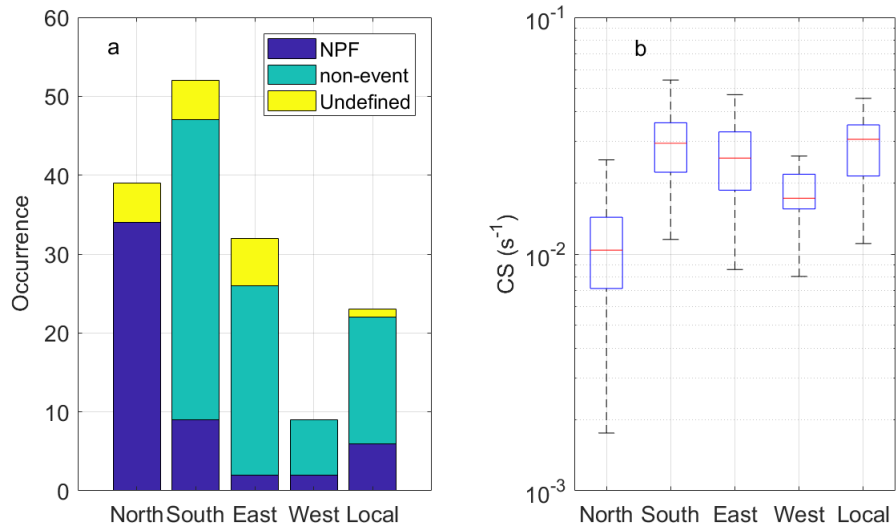


Figure 7: Occurrence of NPF events and non-events under air masses arriving from different directions (a) as well as medians and percentiles of condensation sink (CS, s^{-1}) during the 9:00-11:00 (local time) under different air masses (b) during our observation in summer 2018 and 2019 at UB station. The red line represents the median of the data and the lower and upper edges of the box represent 25th and 75th percentiles of the data, respectively. The length of the whiskers represents 1.5× interquartile range which includes 99.3% of the data. Data outside the whiskers are considered outliers and are marked with red crosses. The time resolution of CS was 8 min.

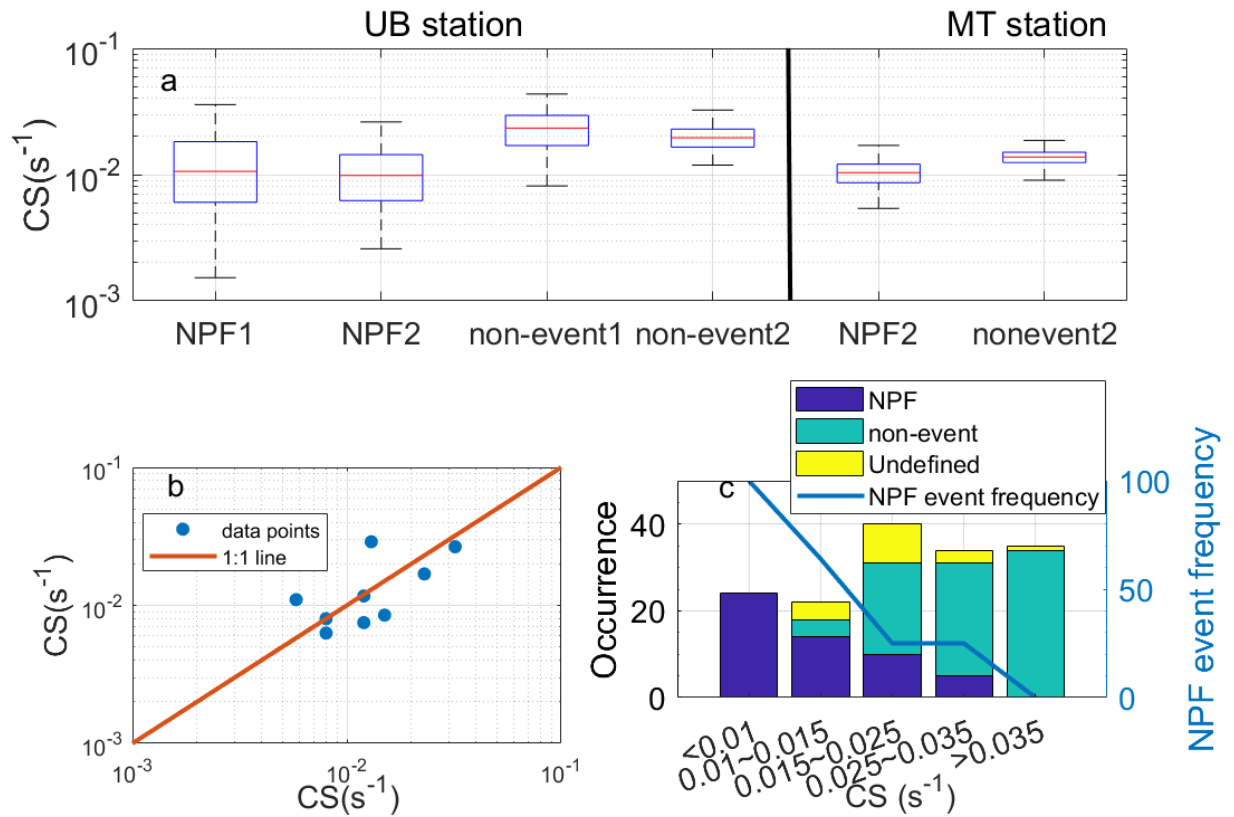


Figure 8: (a) Median and percentiles of condensation sink (CS , s^{-1}) during our observations at both stations. The ‘NPF1’ and ‘non-event1’ referred to NPF and non-event days during summer 2018 and 2019, while ‘NPF2’ and ‘non-event2’ referred to NPF and non-event days during the short-term parallel observation from June 14 to July 14, 2019 at both sites. The red line represents the median of the data and the lower and upper edges of the box represent 25th and 75th percentiles of the data, respectively. The length of the whiskers represents 1.5× interquartile range which includes 99.3% of the data. The time resolution of CS was 8 min. (b) Median CS during the first 2 hours of NPF events on common NPF event days measured at both stations (MT vs. UB). (c) Numbers of NPF event, non-event and undefined days as well as NPF event frequency as a function of CS during our observation in summer 2018 and 2019 at UB station.

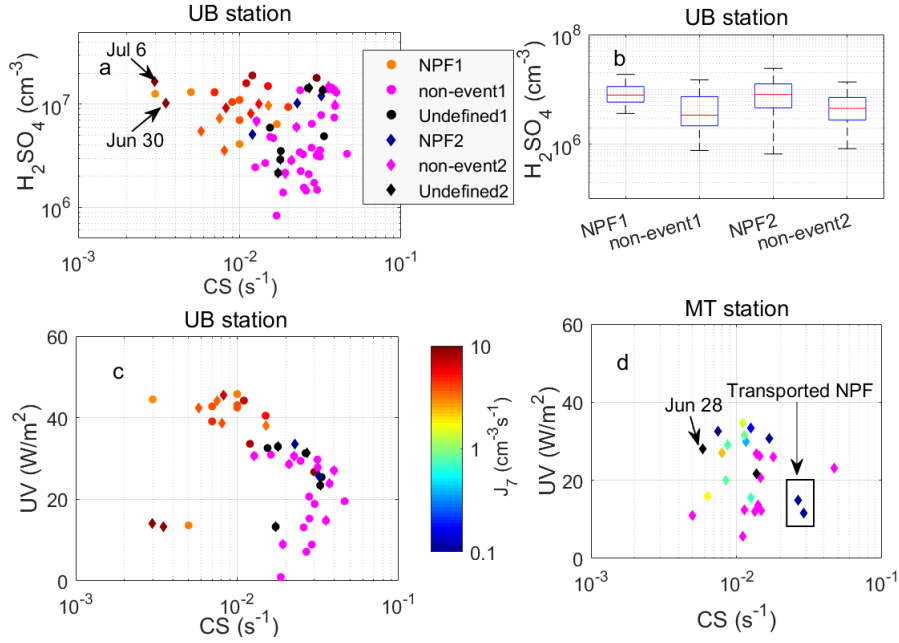


Figure 9: (a) Median condensation sinks (CS , s^{-1}) and H_2SO_4 concentration (SA , cm^{-3}) and (b) solar radiation (UVA+UVB, W/m^2) during the first 2 hours of every NPF event and 9:00-11:00 on every non-event day at UB station. (c) medians and percentiles of H_2SO_4 concentration observed at UB station during the first 2 hours of NPF events and 9:00-11:00 on non-event days. (d) solar radiation (UVA+UVB, W/m^2) during the first 2 hours of every NPF event and 9:00-11:00 on every non-event day at UB station. The ‘NPF1’ and ‘non-event1’ referred to NPF event and non-event days in summer 2018 and 2019 and the ‘NPF2’ and ‘non-event2’ referred to NPF event and non-event days during the observation from June 14 to July 14, 2019. (d) Median condensation sinks (CS , s^{-1}) and solar radiation (UVA+UVB, W/m^2) during the first 2 hours of every NPF event and 9:00-11:00 on every non-event day at MT station. Transported NPF event cases and one non-event day with air masses belonging to west group (Jun 28) were all pointed out in the figure. Size of data points on NPF event days means particle formation rate (J_7 , $cm^{-3}s^{-1}$) when it can be calculated reliably. The time resolution of CS was 8 min at UB station and 4 min at MT station, respectively. The time resolution was 30 min for SA data at UB station and 1h for solar radiation data at both stations.

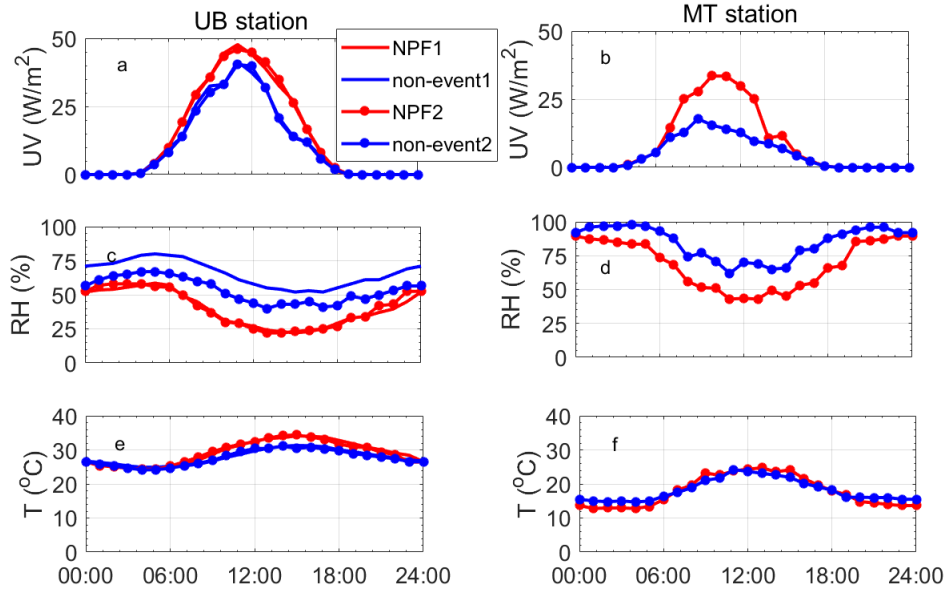


Figure 10: (a, b) Diurnal pattern of solar radiation (UV, W/m²), (c, d) Temperature (T, °C), and (e, f) Relative humidity (RH, %), at UB (left panel) and MT (right panel) stations on both NPF event and non-event days. Time resolutions for all data points here were 1h. [The ‘NPF1’ and ‘non-event1’ referred to NPF event and non-event days in summer 2018 and 2019 and the ‘NPF2’ and ‘non-event2’ referred to NPF event and non-event days during the observation from June 14 to July 14, 2019.](#)

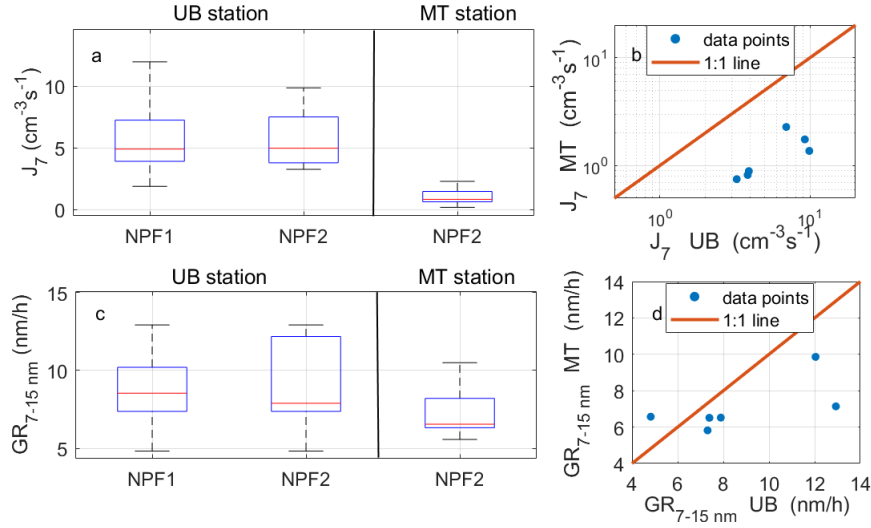


Figure 11: Median and percentages of particle formation rates of 7 nm (J_7 , cm^3s^{-1}) (a) and particle growth rates from 7 to 15 nm ($GR_{6-15 \text{ nm}}$, nm/h) (c) measured at both stations during our observation as well as comparison between J_7 (b) and $GR_{6-15 \text{ nm}}$ (d) of common NPF events. The red line represents the median of the data and the lower and upper edges of the box represent 25th and 75th percentiles of the data, respectively. The length of the whiskers represents 1.5× interquartile range which includes 99.3% of the data. The ‘NPF1’ and ‘non-event1’ referred to NPF event and non-event days in summer 2018 and 2019 and the ‘NPF2’ and ‘non-event2’ referred to NPF event and non-event days during the observation from June 14 to July 14, 2019.

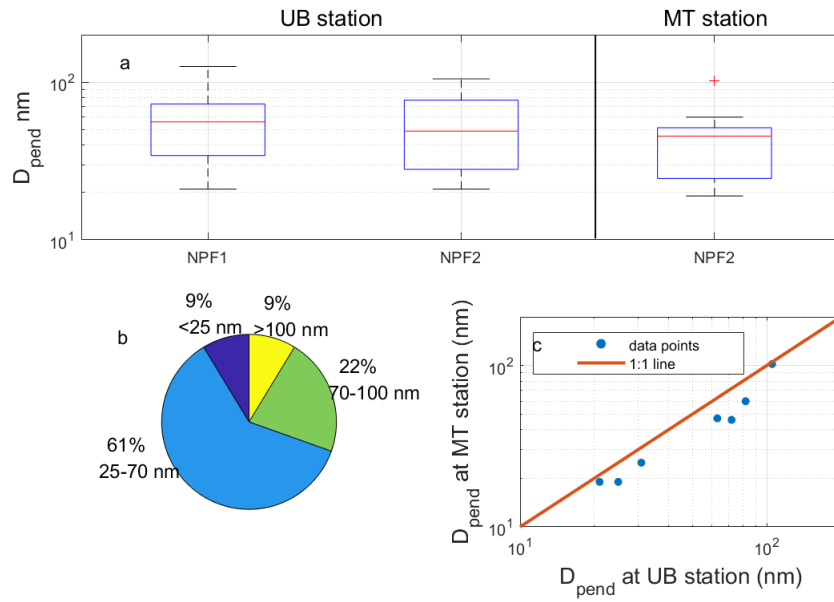


Figure 12: (a) Median and percentiles of end diameters (D_{pend} , nm) of NPF events measured at both sites. The red line represents the median of the data and the lower and upper edges of the box represent 25th and 75th percentiles of the data, respectively. The length of the whiskers represents 1.5 \times interquartile range which includes 99.3% of the data. The ‘NPF1’ and ‘non-event1’ referred to NPF event and non-event days in summer 2018 and 2019 and the ‘NPF2’ and ‘non-event2’ referred to NPF event and non-event days during the observation from June 14 to July 14, 2019. (b) Frequencies of end diameters in the size range of smaller than 25 nm, 25-70 nm, 70-100 nm and above 100 nm during our observation at UB station in summer 2018 and 2019. (c) Comparison between end diameters of common NPF events at both stations.

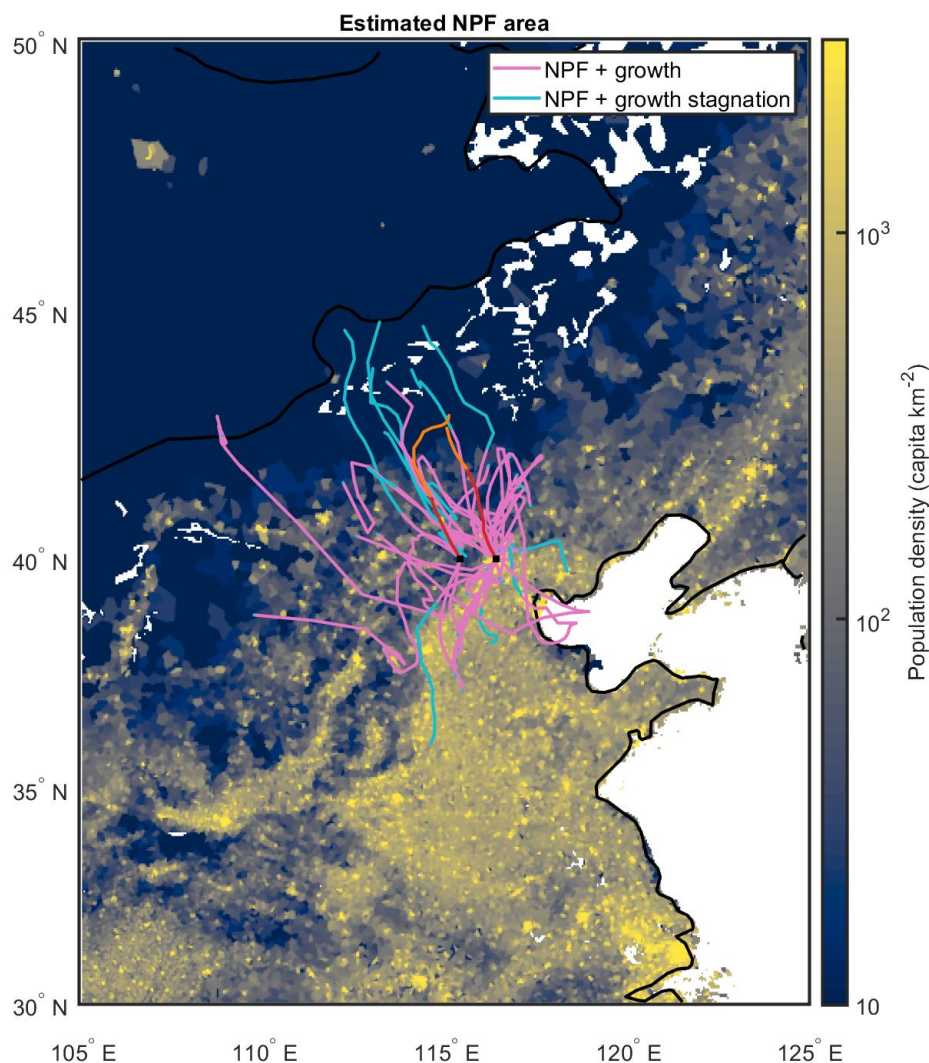


Figure 13: Spatial extent of the area where new particle formation events are estimated to have taken place based on air mass back trajectories and the observed NPF events at both sites. Each line represents a single NPF event and extends to the point beyond which continuation of the mode formed in an NPF event was no longer observed at the measurement site. In other words, if an air mass is located outside the area roughly outlined by the colored lines during the typical onset time of NPF and then transported to our measurement sites, NPF is unlikely to have occurred in said air mass. The lines change color from pink to light blue if the observed NPF event enters a stage of growth stagnation, which can indicate a less favorable environment for the formation and growth of new particles. The lines for the case study day of June 30, 2019 are marked with red and change color to orange

1189 [if growth stagnation occurs. The lines are overlaid on top of a population density map](#)
1190 [\(Gridded Population of the World; GPWv4.10; CC BY 4.0\), which is used to illustrate the](#)
1191 [level of anthropogenic activities and emissions.](#)

1192

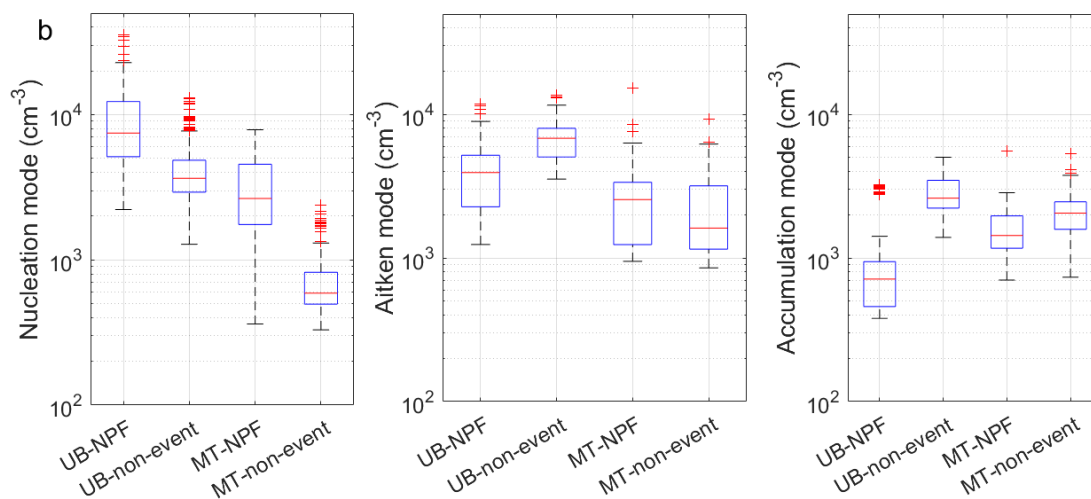
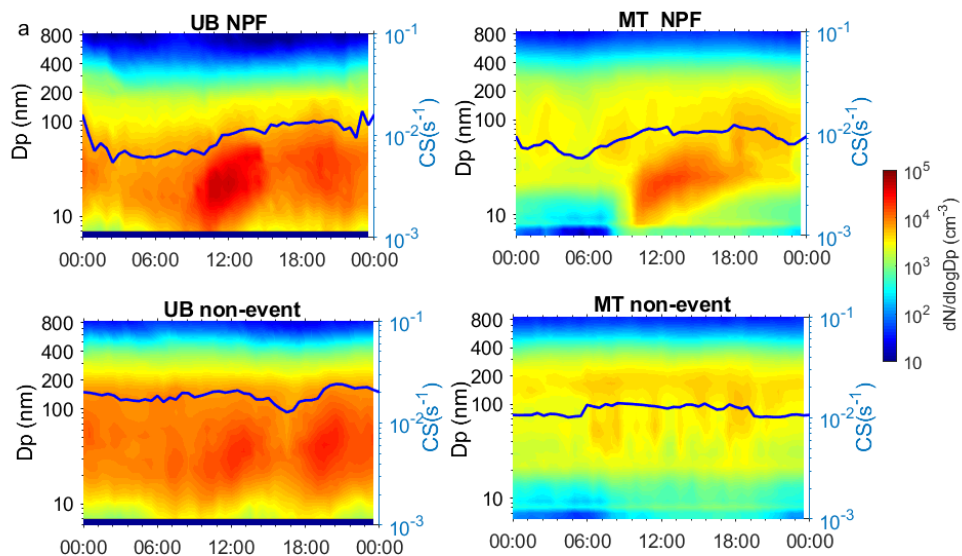
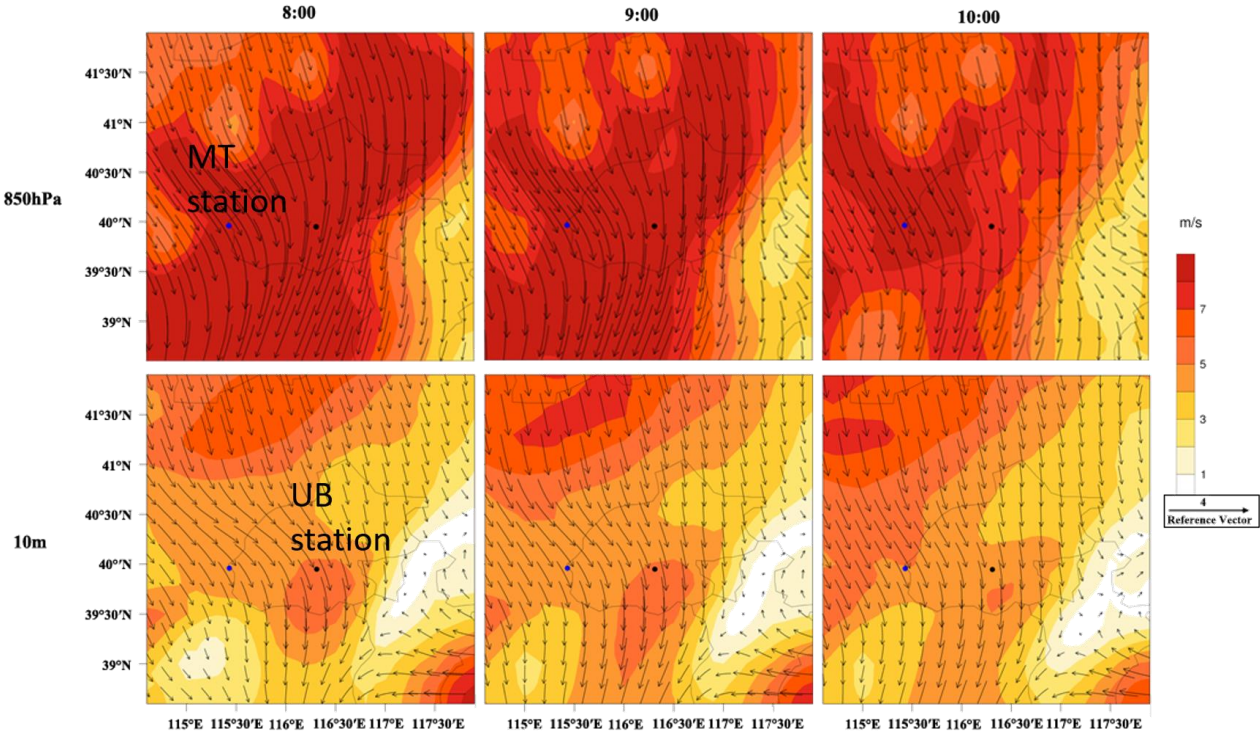


Figure 14: (a) Median particle number size distribution as well as CS (blue lines) on NPF event and non-event days at UB (left panel) and MT (right panel) stations and (b) median and percentiles of nucleation, Aitken and accumulation modes particle number concentration on NPF event and non-event days during our observation from June 14 to July 14, 2019 at both stations. The red line represents the median of the data and the lower and upper edges of the box represent 25th and 75th percentiles of the data, respectively. The length of the whiskers represents 1.5× interquartile range which includes 99.3% of the data. Data outside the whiskers are considered outliers and are marked with red crosses.

1204



1205

1206

1207

1208

1209

[Figure 15: Wind distribution at 8:00, 9:00 and 10:00 on June 30, 2019 at 10 m above the ground level \(lower panel\) and 850 hPa \(close to the altitude of MT station, upper panel\). The blue and black points on the figures represent MT and UB stations, respectively.](#)

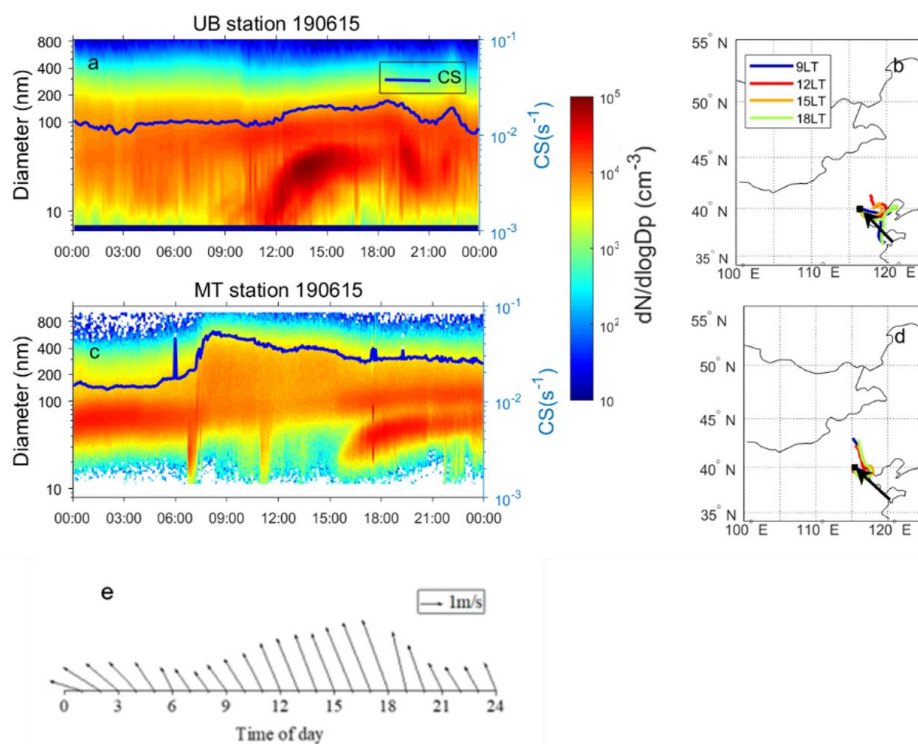


Figure 416: Time series of particle number size distribution, CS (blue lines) and air masses arrived at UB (upper panel) and MT (bottom panel) stations as well as wind conditions at MT station on June 15, 2019. Time resolution for particle number size distribution data and CS were both 8 min at UB station and 4 min at MT station, respectively. Time resolution for wind condition data was 1h at MT station. The arrows in the figure denotes directions of prevailing air masses before arriving at both stations during 9:00-15:00 LT.

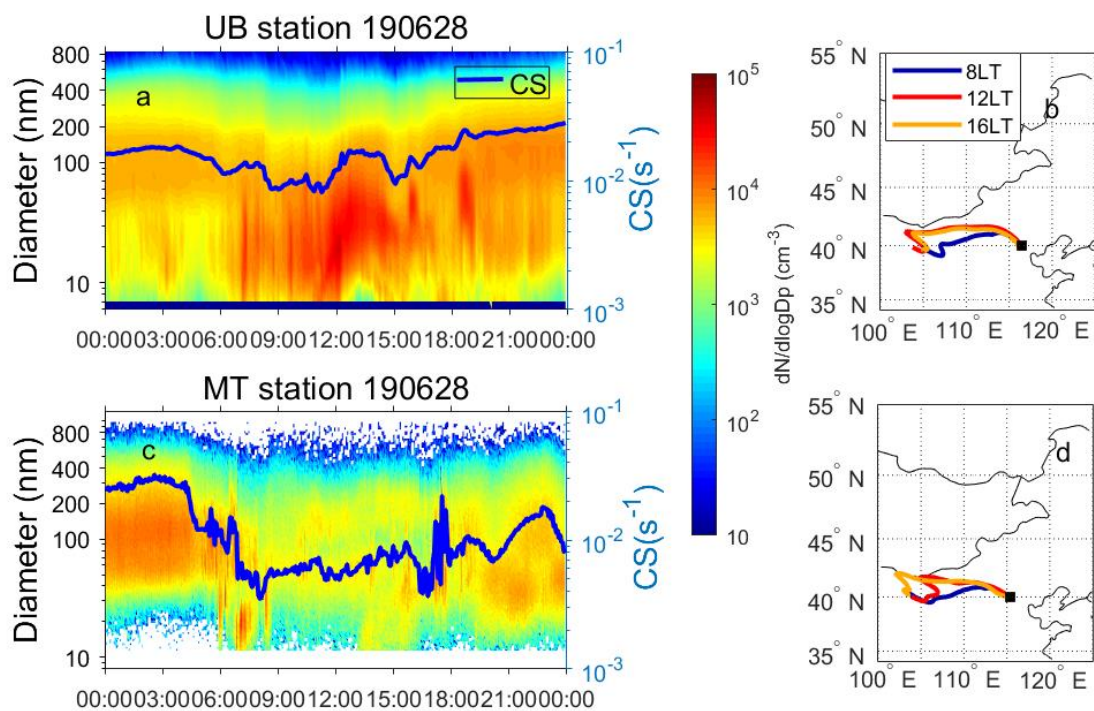


Figure 127: Time series of particle number size distribution, CS and air masses arrived at UB (upper panel) and MT (bottom panel) stations on June 28, 2019. Time resolution for particle number size distribution data and CS were both 8 min at UB station and 4 min at MT station, respectively.

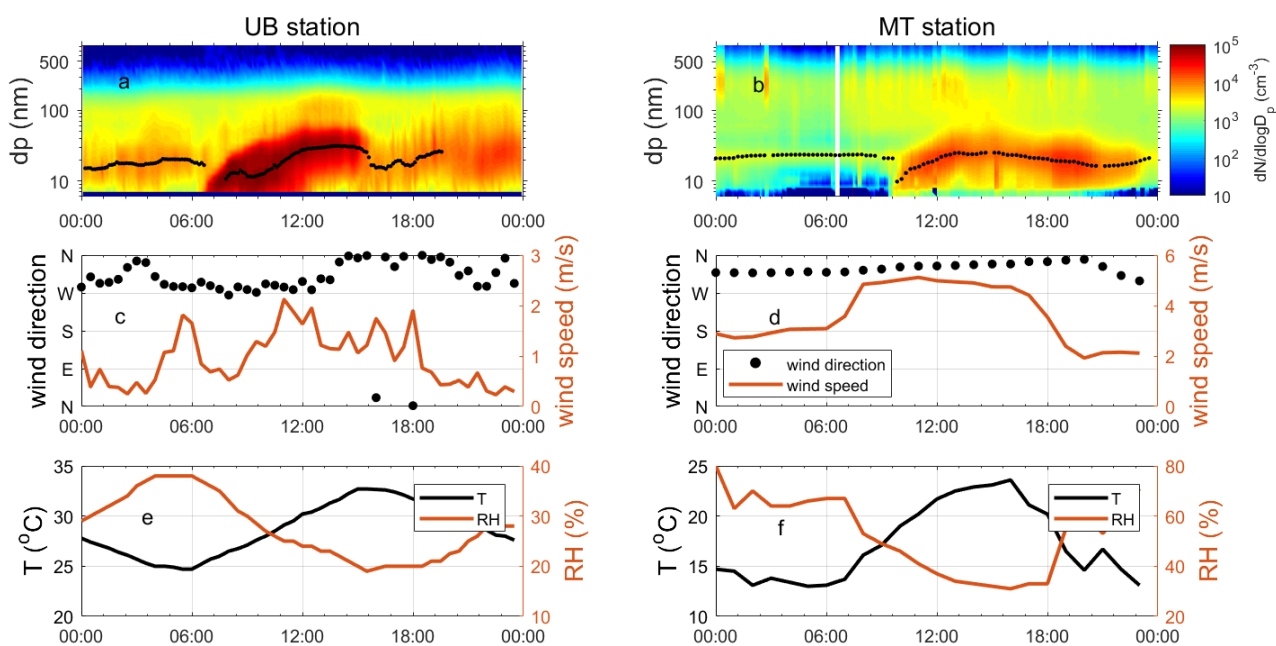


Figure 18: Time series of particle number size distribution and mode diameters (a, b), wind

1225 speed and direction (c, d), temperature and RH (e, f) measured at UB (left panel) and MT
1226 (right panel) on June 30, 2019.